ADVANCING EARTH AND SPACE SCIENCE

Earth and Space Science

RESEARCH ARTICLE
10.1029/2022EA002472

Key Points:
- A sea ice digital elevation model (DEM) is derived from satellite radar data and validated over old and rough sea ice in the Weddell Sea
- Three-dimensional (3D) sea ice patterns are calculated from the sea ice DEM, and are quantitatively analyzed with bathymetry
- Sea ice DEM helps advance the understanding of sea ice processes and facilitates applications such as ship navigation in ice-covered waters

Supporting Information:

Supporting Information may be found in the online version of this article.

Correspondence to:

L. Huang,
huang@ifu.baug.ethz.ch

Citation:

Huang, L., Hajnsek, I., & Nghiem, S. V. (2022). Sea ice elevation in the Western Weddell Sea, Antarctica: Observations from field campaign. *Earth and Space Science*, *9*, e2022EA002472. https://doi.org/10.1029/2022EA002472

Received 27 JUN 2022
Accepted 3 AUG 2022

Author Contributions:

Conceptualization: Irena Hajnsek, Son V. Nghiem
Formal analysis: Lanqing Huang, Son V. Nghiem
Funding acquisition: Irena Hajnsek, Son V. Nghiem
Investigation: Lanqing Huang
Methodology: Lanqing Huang, Son V. Nghiem
Project Administration: Irena Hajnsek, Son V. Nghiem

Sea Ice Elevation in the Western Weddell Sea, Antarctica: Observations From Field Campaign

Lanqing Huang[1], **Irena Hajnsek**[1,2], **and Son V. Nghiem**[3]

[1]Institute of Environmental Engineering, Swiss Federal Institute of Technology in Zürich (ETH), Zürich, Switzerland, [2]Microwaves and Radar Institute, German Aerospace Center (DLR), Wessling, Germany, [3]Jet Propulsion Laboratory, California Institute of Technology, Pasadena, CA, USA

Abstract Sea ice elevation is crucial in the characterization of three-dimensional (3D) sea ice patterns, providing physical insights to advance sea ice dynamic models. Moreover, how sea ice elevation may be related to the ocean geophysical environment is still a significant knowledge gap, especially in Antarctica. A radar theory relating electromagnetic scattering mechanisms to sea ice elevation over old and deformed rough ice has been reported in a prior companion paper. This follow-up paper presents the validated model function and synthetic aperture radar (SAR)-retrieved sea ice elevations based on the field data acquired during the Operation IceBridge and TanDEM-X Antarctic Science Campaign. A high-resolution sea ice digital elevation model (DEM) is generated extensively over a 19 × 450 km sector in the Western Weddell Sea, achieving a good accuracy with a low root-mean-square error of 0.23 m. From the SAR-retrieved sea ice DEM, 3D sea ice patterns including roughness height, auto-correlation lengths, correlation ellipticity, and orientation angles are calculated over the old and deformed rough sea ice. The 3D sea ice patterns give a comprehensive characterization of sea ice topography in the Western Weddell Sea and show the potential to be used for understanding sea ice formation processes in the Antarctic.

Plain Language Summary Sea ice elevation provides essential information on characterizing sea ice features in three dimensions (3D) and relates to the ocean geophysical environment in the Antarctic. Synthetic aperture radar (SAR) provides a novel capability to characterize sea ice in 3D over a large coverage area across the ocean surface regardless of weather and darkness. This paper presents a method to retrieve sea ice elevations based on SAR imagery. A high-resolution map of sea ice elevation for old and rough ice is generated extensively over a wide sector in the Western Weddell Sea. Numerous sea ice 3D features are derived from the sea ice elevation map and show potential to provide geophysical insights into sea ice formation processes in the Antarctic.

1. Introduction

Sea ice surface elevation, including ice freeboard and snow thickness above the local sea level, is formed by features such as floe edges, pressure ridges, ice rafting, hummocks, and thick ice growth (Weeks & Ackley, 1986). These features define the sea ice topography, which can be characterized by a sea ice digital elevation model (DEM). Sea ice DEM is a critical parameter for sea ice dynamic modeling to determine the air-ice drag coefficient and the momentum flux (Andreas et al., 1993; Guest & Davidson, 1991). Moreover, characterization of sea ice topography across the vast expansion of the sea ice cover, together with the assumed values of sea ice density, snow density, and water density, can be used to estimate sea ice volume (Markus et al., 2011), which is a key indicator to represent the implications of sea ice change that are influenced by climate change (Kurtz & Markus, 2012). Sea ice DEM can also be used to map regional variations and to perform trafficability analyses that can help ship navigation (Dammann et al., 2017; Hibler III & Ackley, 1975).

Currently, the most precise vertical height accuracy of sea ice topography is obtained by laser altimeters on an airborne or spaceborne platform (Abdalati et al., 2010; Dierking, 1995; Farrell et al., 2011; Granberg & Leppäranta, 1999; Schutz et al., 2005). However, a major limitation of the laser altimeter is the small-spatial coverage, which is commonly in the range of 200–2,000 m. Synthetic aperture radar (SAR) has become an invaluable remote sensing sensor with a wide-spatial coverage over tens of kilometers and has high spatial resolution capabilities at meter scales. A SAR actively illuminates scenes at a suitable frequency regardless of cloud cover and darkness, and acquires scattering signals carrying information about sea ice characteristics

Earth and Space Science

10.1029/2022EA002472

Supervision: Irena Hajnsek, Son V. Nghiem
Validation: Lanqing Huang
Visualization: Lanqing Huang
Writing – original draft: Lanqing Huang
Writing – review & editing: Irena Hajnsek, Son V. Nghiem

(Carsey, 1992). SAR backscatter coefficient has been related with sea ice root-mean-square (RMS) height measurements from laser altimeters (Dierking et al., 1997; Peterson et al., 2008). Haas et al. (1999) retrieved the frequency and height distributions of Antarctic pressure ridge sails from the C-band SAR backscatter coefficient in Antarctica. With the development of SAR polarimetric techniques, numerous studies have demonstrated good correlations between Arctic sea ice roughness and polarimetric SAR features such as coherence magnitude between right-right and left-left polarizations (Fors et al., 2015) and cross-polarization ratio (Cafarella et al., 2019).

Sea ice properties in the Arctic and Antarctic can be significantly different due to diverse growth conditions (Gloersen, 1992; Walsh, 2009). Recent tests have shown that the phase altimetry using Reflected Global Navigation Satellite System data can potentially measure sea ice thickness of smooth and thin sea ice (Li et al., 2017; Yan & Huang, 2019) that has a low elevation around 0.1 m above the open seawater surface. Unlike the thin and fragile ice near the sea ice edge in the Arctic, Antarctic sea ice can have high elevations corresponding to thick ice even near the sea ice edge, such as in the Weddell Sea (Ackley, 1979). Markus et al. (2011) also suggested that storms can cause significant sea ice deformation and pronounced average roughness in the East Antarctic region where the extent of the sea ice is only ∼300 km. With the objective to investigate sea ice topography across the extensive expansion in the Antarctic, the Operation IceBridge and TanDEM-X Antarctic Science Campaign (OTASC) was successfully conducted in 2017.

OTASC offered a unique opportunity to obtain sea ice DEMs over a large spatial scale from both optical and SAR sensors in the Antarctic (Nghiem et al., 2018). The Operation IceBridge (OIB) airborne mission carried various instruments that acquired different data sets. Among them, a stereo camera was used to reconstruct a high-resolution map of sea ice topography using photogrammetric techniques (Dotson & Arvesen, 2012, updated 2014). TanDEM-X, a single-pass SAR interferometer developed by the German Aerospace Center (Krieger et al., 2007), acquired high-resolution co-registered single-look complex data extensively during OTASC. With TanDEM-X's single-pass nature, elevation retrieval over sea ice becomes promising despite the dynamic nature of sea ice (Dierking et al., 2017; Yitayew et al., 2018). However, the penetration of microwaves into snow and low-salinity ice, as well as the operated TanDEM-X height sensitivity (i.e., Height-of-Ambiguity), limit the accuracy of interferometric SAR (InSAR)-derived sea ice elevation. Huang and Hajnsek (2021) observed a distinct elevation difference of around 1.09 m between the InSAR-derived DEM and the reference DEM from OTASC data over the snow-covered deformed ice, suggesting a demand for new algorithms that can correct the elevation discrepancy.

In the theoretical study of the Antarctic sea ice (Nghiem et al., 2022), an advanced electromagnetic model for old ice (OI) and rough deformed ice (RI) has been developed, based on the first principle of Maxwell's equations, to establish an inverse relationship among the SAR co-polarimetric (coPol) coherence $|\rho|$ and sea ice elevation. Following the physical principles and the protocol to retrieve sea ice DEM from Nghiem et al. (2022), this paper presents a sea ice DEM for the two ice types (i.e., OI and RI) over a 19 × 450 km sector in the Western Weddell Sea using polarimetric and interferometric techniques from single-pass InSAR imagery. The results show that coPol coherence carries essential information on sea ice elevation and can be combined with interferometry to improve sea ice DEM retrieval accuracy. Note that the term "elevation" throughout the paper refers to the elevation of ice, including the snow cover relative to the local sea level. From the SAR-retrieved sea ice DEM, 3D sea ice patterns in terms of RMS height, auto-correlation lengths in long and short axes, correlation ellipticity, and orientation angles of sea ice elevation are calculated and analyzed for the two types of sea ice (i.e., the OI and the RI). Statistical analyses indicate invariant sea ice topographic features across certain specific areas. We also discuss the sea ice patterns in 3D with geophysical conditions in terms of bathymetric depth and aspect angle. These analyses give the first observations of the relationship among sea ice 3D topographic features, providing new physical insights to examine sea ice formation processes in the Antarctic.

The main objective of this paper is to retrieve OI and RI elevation and characterize sea ice 3D patterns from SAR imagery across a broad spatial coverage over the Western Weddell Sea. The organization of the paper includes data sets description in Section 2, data processing in Section 3, sea ice classification in Section 4, sea ice DEM retrieval in Section 5, generation and analyses of sea ice 3D patterns in Section 6, and conclusion in Section 7.

10.1029/2022EA002472

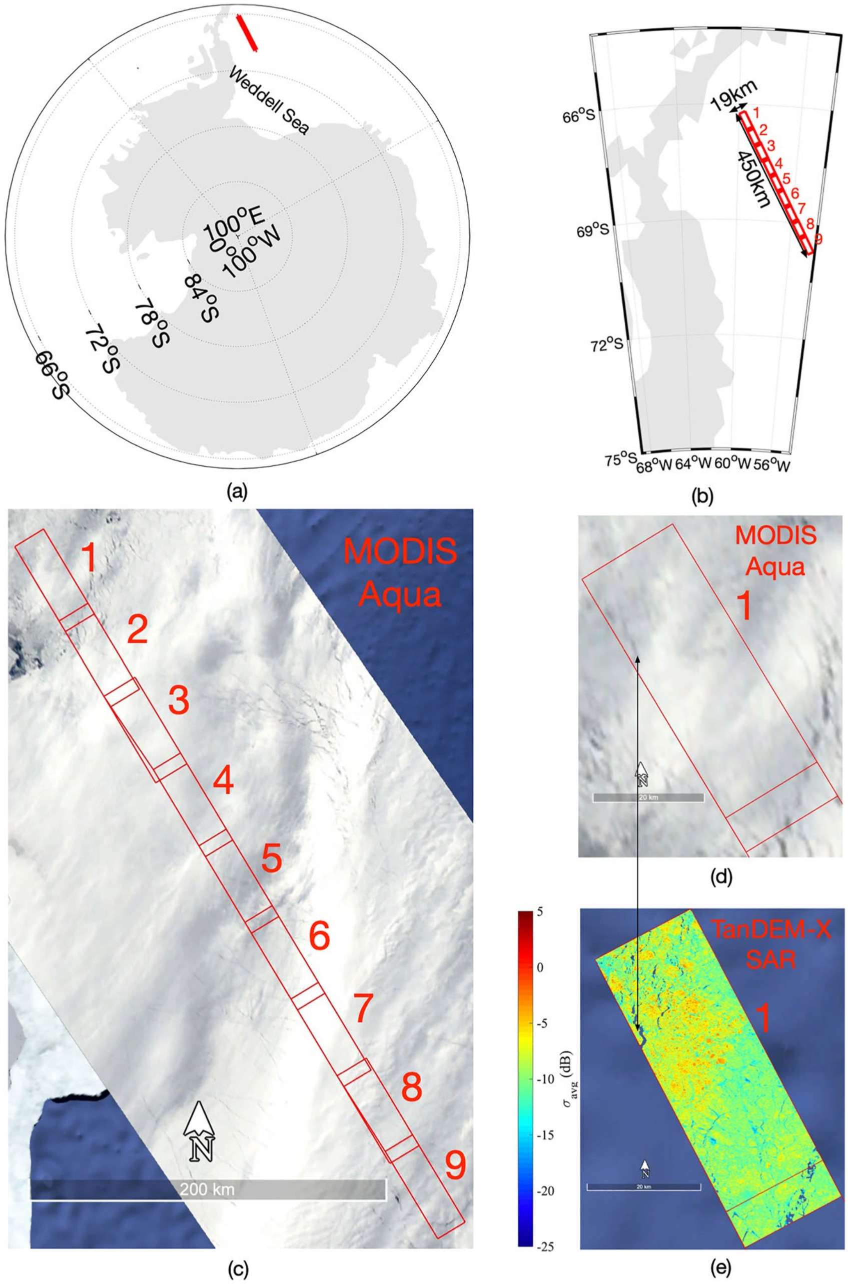

Figure 1. Demonstration of the study area (Scenes 1–9). (a) and (b) Geo-location of the study area. (c) Optical MODIS Aqua images over the study area. (d) Optical MODIS Aqua image over Scene 1. (e) TanDEM-X SAR image over Scene 1; the pseudo color represents the averaged noise-subtracted backscattering intensity of HH and VV polarizations.

2. Data Sets

2.1. Study Area

The study area is located in the Western Weddell Sea, Antarctica. An overview of the geo-location is presented in Figures 1a and 1b, where the spatial coverage of the study area is around 450 × 19 km. The true-color optical image over the study area captured from MODIS Aqua satellite (NASA Worldview Snapshots, 2000) shows cloud cover at UTC 19:15 October 29, 2017 (see Figure 1c). A pair of coordinated images from MODIS Aqua and TanDEM-X SAR covering Scene 1 are presented in Figures 1d and 1e, respectively. Sea ice in this area is

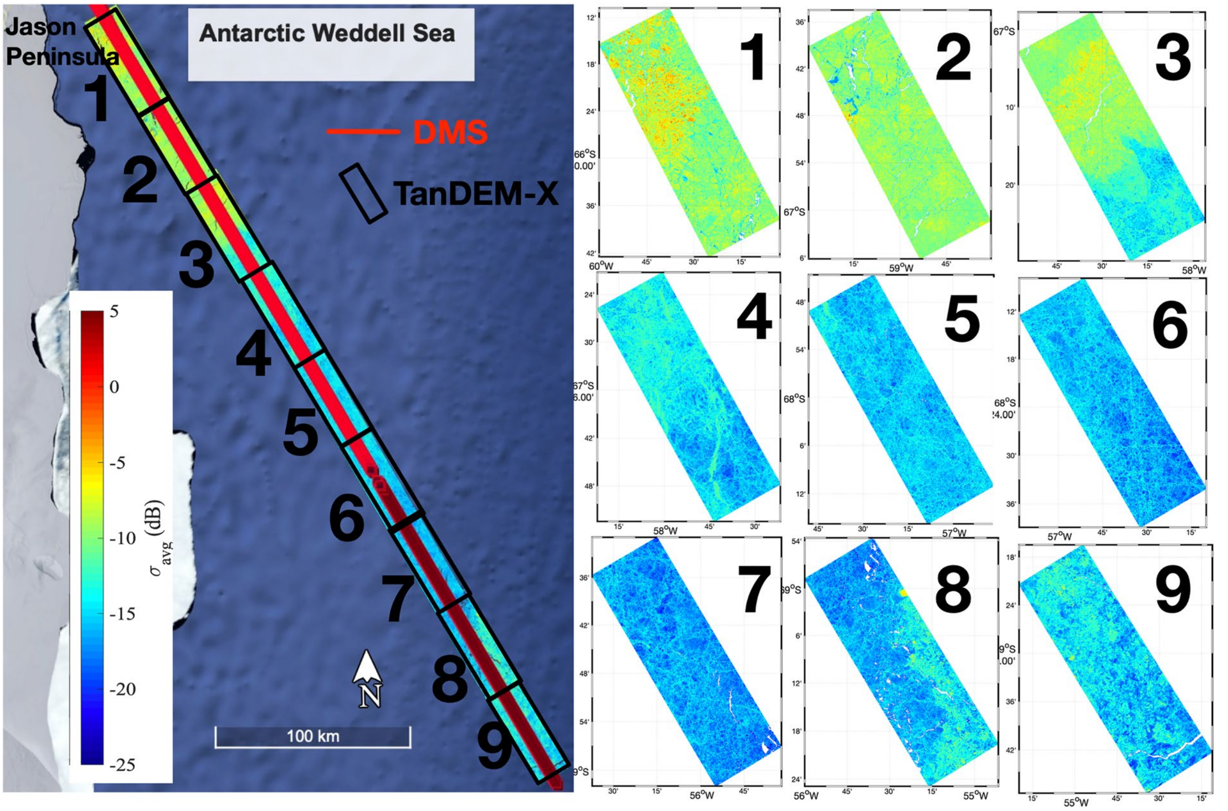

Figure 2. The coordinated data sets over the study area: 9 scenes of TanDEM-X noise-subtracted backscattering intensity images overlaid by the flight track of Operation IceBridge (OIB) aircraft. The pseudo color represents the averaged synthetic aperture radar (SAR) backscattering intensity in HH and VV polarizations.

mostly invisible from the optical sensor (i.e., MODIS Aqua image) due to the cloud covers, whereas the SAR (i.e., TanDEM-X intensity image) is capable of observing the sea ice regardless of the cloud cover.

2.2. Field Campaign

The coordinated campaign named OTASC was conducted between the TanDEM-X satellite and the OIB aircraft over the Western Weddell Sea, Antarctica, on October 29, 2017 (Nghiem et al., 2018). Satellite and aircraft data acquisitions were closely coordinated to obtain collocated and contemporaneous data sets for sea ice observations during OTASC.

Figure 2 shows the OIB airborne flight track (red line) overlaid on nine TanDEM-X SAR images, where the pseudo color indicates the average of the noise-subtracted SAR backscattering intensity of HH and VV polarizations. The noise-subtraction method will be described in Section 4. Henceforth, the nine SAR images will be mentioned as Scenes 1–9.

2.2.1. SAR Data

The spaceborne TanDEM-X satellite, equipped with a single-pass SAR interferometer, can acquire two images (i.e., InSAR pair) with milliseconds of temporal lag (Krieger et al., 2007). In this study, the InSAR pairs are co-registered single-look slant-range complex (CoSSC) products with dual-polarization (HH and VV) in StripMap mode and are employed to generate sea ice DEMs by interferometric processing. The data over the study area were collected in the bistatic mode from UTC 23:40 to 23:41 on October 29, 2017. For each acquisition, the incidence angle of the scene center is ∼34.9°, and the pixel spacing is around 0.9 × 2.7 m in slant range and azimuth. For each InSAR pair, the effective perpendicular baseline $b_{\perp}$ and the along-track baseline b_{al} are about 175.7 and 201.9 m, respectively. The height-of-ambiguities for the nine scenes vary from 32.5 to 34.0 m.

10.1029/2022EA002472

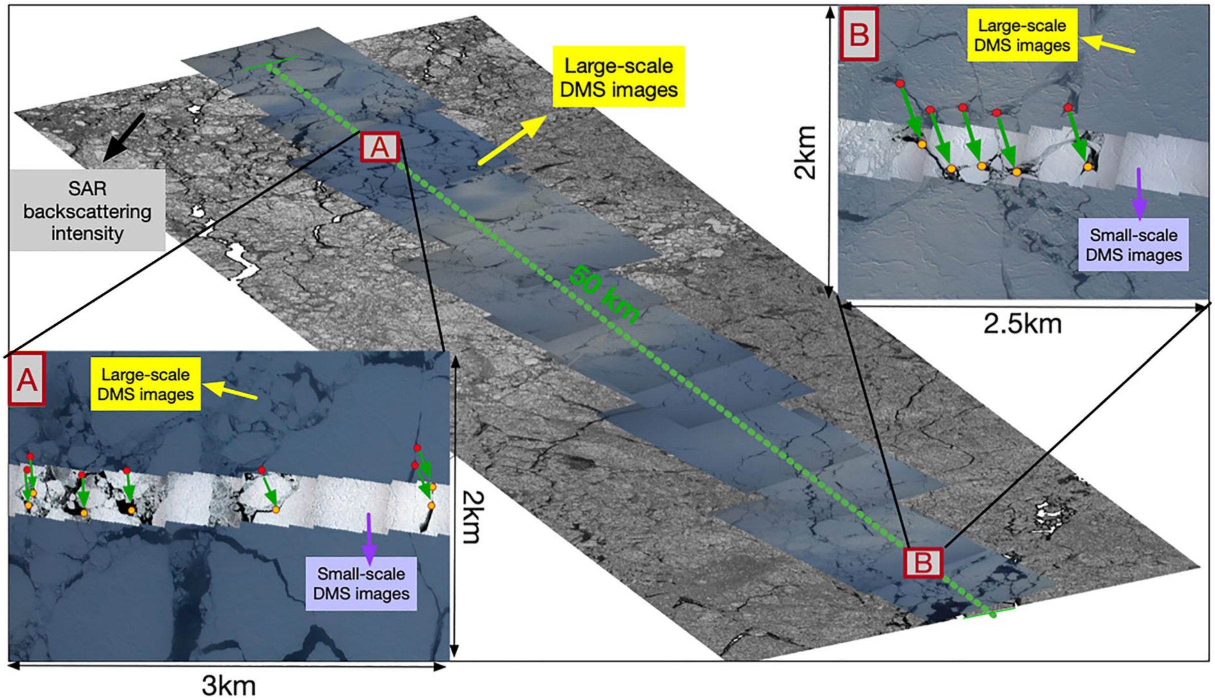

Figure 3. Representation of synthetic aperture radar (SAR) intensity image, large-scale digital mapping system (DMS) images, and small-scale DMS images of Scene 1. The green dash line indicates the 50 km transect overlaid by DMS digital elevation models (DEMs). Sub-image A and sub-image B are zoomed-in from area A and area B, where the small-scale DMS images (acquired at UTC 17:50 on October 29, 2017) are superimposed on the large-scale DMS images (acquired at UTC 22:05 on October 29, 2017). The red and orange dots denote the selected reference pairs from the large- and small-scale DMS images, respectively. The green arrows denote the "shift-vectors" used for estimating drift velocity.

2.2.2. Optical Data

NASA airborne OIB mission equipped with the digital mapping system (DMS) captures optical camera images (Dominguez, 2010, updated 2018) to generate sea ice DEMs (Dotson & Arvesen, 2012, updated 2014).

The DMS camera captures natural color and panchromatic images with spatial resolution ranging from 0.015 to 2.5 m depending on the flight altitude (Dominguez, 2010, updated 2018). The DMS camera acquired two types of image during separate airborne overflights: large- and small-scale DMS images covering an area around 5.8 × 8.8 km and 400 × 400 m, respectively. Over the study area (Scenes 1–9, labeled in Figure 2), the collection of large-scale DMS images took place from UTC 21:28 to 22:07 on October 29, 2017, and the small-scale DMS images were captured on the same date from UTC 17:45 to 18:44. Scene 1 is presented as an example in Figure 3 where the large-scale DMS images are superimposed on the TanDEM-X SAR intensity image. The transect overlaid by small-scale DMS images is delineated along the green line in Figure 3, where the small-scale DMS images of areas A and B are enlarged in sub-images A and B as two examples.

Each DMS DEM was generated from the small-scale DMS image by photogrammetric technique (Dotson & Arvesen, 2012, updated 2014); therefore, the time stamp and the spatial coverage of DMS DEM are identical to the small-scale DMS image. DMS DEM characterizes sea ice topography with a spatial resolution of ~40 × 40 cm. The accuracy of DMS DEMs is ~0.2 m (Dotson & Arvesen, 2012, updated 2014). As the acquisition took place from UTC 17:45 to 18:44 on October 29, 2017, over the study area, there was a time difference of 5–6 hr between the DMS DEMs and the TanDEM-X SAR acquisitions. In the OTASC experiment plan, information on sea ice motion was carefully considered to ensure that OIB aircraft data could be collected within the ground coverage of TanDEM-X SAR swaths so that data co-registration would be possible. The pre-planned operation of the OIB aircraft in coordination with TanDEM-X tracks from orbit ephemeris data was successfully conducted with the expertise of the NASA OIB flight team.

3. Data Processing

3.1. DMS Post-Processing

DMS DEMs are reprojected from Antarctic Polar Stereographic to World Geodetic System 1984 (WGS84) spatial reference and geocoded into SAR coordinates with the same resolution as the multilook TanDEM-X image ($\sim$10 × 10 m in range and azimuth) using the GAMMA software (Werner et al., 2000). The DMS DEMs are then calibrated to the local sea level by selecting the water surface reference from DMS images. Note that the DMS DEM measures sea ice elevation including the snow cover on top.

3.2. Data Co-Registration

Sea ice can drift from 0 to tens-of-centimeters per second depending on the ice type and external forces (e.g., wind and current) (Dierking et al., 2017). Therefore, it is necessary to employ data co-registration to compensate for the sea ice movement during the time difference of 5–6 hr between the DMS DEMs and TanDEM-X acquisitions.

Over the study area, sea ice backscattering intensity tends to be lower toward the southeastern direction (from Scenes 1–9), shown in Figure 2, corresponding to the thinner and smoother sea ice (Nghiem et al., 2016). Strong dynamics in the thinner ice area would lead to severe misregistration between the DMS DEMs and TanDEM-X. Besides, a lack of pronounced patterns in the thinner ice area impedes selecting distinguishable ice features for co-registration. In favorable conditions, advanced co-registration algorithms can be applied to precisely estimate the shift over the thinner ice area (Kræmer et al., 2015). However, an effective co-registration certainly depends on the quality of the data sets. Unexpected weather conditions (e.g., fog, haze formation) during the acquisition degraded the imaging quality from the DMS optical sensor and thereby inflicted an excessive difficulty on the data co-registration. As a result, to ensure reliable performance, Scene 1 is used as the basis for the data co-registration due to the inherently low dynamics of the thicker ice together with the best quality of DMS images.

Co-registration between the DMS DEMs and TanDEM-X images contains two steps: (a) estimating ice drift velocity and (b) compensating the shift distance by multiplying the ice drift velocity with the temporal gap of the two sensors. As shown in Figure 3 sub-images A and B, sea ice features are evident in both large-scale DMS images and small-scale DMS images, which were acquired about 4 hr 15 min (Δt_1) later. In this case, the distance of ice drift can be estimated by tracking the movement of distinguishable features (e.g., pieces of sea ice or leads) from the large- and small-scale DMS image. In Scene 1, the 50 km transect (green dash line in Figure 3) overlaid by DMS flight track is divided into 50 segments. Each segment contains 1 × 100 pixels in range and azimuth corresponding to about 1 km length. For every segment, several pairs of distinguishable features are labeled (see the red and orange dots in Figure 3 sub-images A and B), and their spatial-shift distance during Δt_1 are extracted. Then, "shift-velocity vectors" can be derived in both azimuth and range directions in radar coordinate, shown as the green arrows in Figure 3, sub-images A and B. For each segment, co-registration can be conducted by multiplying the "shift-velocity vector" with the temporal gap (Δt_2 = 5 hr 53 min) between the DMS DEMs and TanDEM-X acquisition.

Since the co-registration above is performed by compensating the shift in range and azimuth direction, residual misregistration still exists for the sea ice undergoing non-linear movement or rotation during Δt_2. After a careful check of all 50 segments, 11 segments are excluded due to the residual misregistration. Therefore, a refined co-registered data set, including 39 co-registered segments, will be used for verification and validation.

3.3. SAR Interferometry

For TanDEM-X CoSSC InSAR products, the co-registration and common spectral band filtering in range and azimuth have already been processed (Duque et al., 2012). The remaining interferometric processing includes interferogram generation, flat earth removal, interferogram filtering, low-coherence area mask, phase unwrapping, and phase-to-height conversion. During the processing, a 4 × 12 multi-looking window is used in azimuth and slant range, corresponding to about 10 × 10 m spatial size. The details can be found in Huang and Hajnsek (2021).

Following the above InSAR processing, the magnitude of interferometric coherence $|\tilde{\gamma}_{\text{InSAR}}|$ are derived for HH and VV polarization and then averaged, shown in Figure 4. The pixels with $|\tilde{\gamma}_{\text{InSAR}}|$ less than 0.3 are masked out as water area and will not be considered in the following processing. The InSAR phase center heights for HH and VV

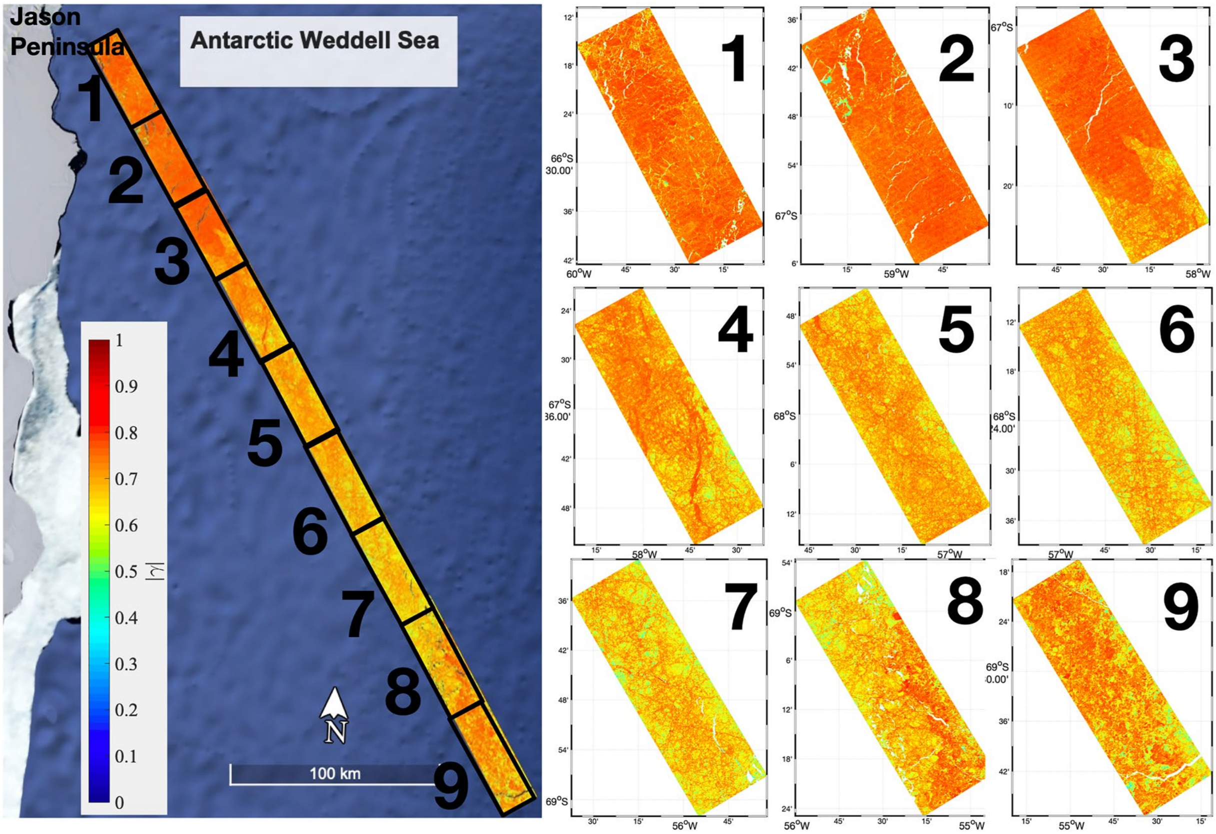

Figure 4. Averaged magnitude of interferometric coherence $|\tilde{\gamma}_{\mathrm{InSAR}}|$ between HH and VV polarization.

polarization are generated separately and then averaged (shown in Figure 5) to cancel potential system noise. For both $|\tilde{\gamma}_{\mathrm{InSAR}}|$ and InSAR phase center heights, the differences between the HH and VV polarization are marginal.

3.4. SAR Polarimetry

SAR polarimetry provides information on the scattering processes and is a valuable tool to characterize sea ice properties. The complex coPol coherence measured from SAR can be affected by system noise (Nghiem et al., 1995b). The complex coPol coherence $\tilde{\rho}_n$ from SAR observations is given by Lee and Pottier (2009).

$$\tilde{\rho}_n = |\rho_n| \cdot e^{i\angle\rho} = \frac{< s_{\mathrm{VV}} s_{\mathrm{HH}}^* >}{\sqrt{< s_{\mathrm{VV}} s_{\mathrm{VV}}^* >< s_{\mathrm{HH}} s_{\mathrm{HH}}^* >}} \tag{1}$$

where s_{HH} and s_{VV} are single-look complex images in HH and VV polarization, respectively, $\angle\rho$ is the coPol phase, and $|\rho_n|$ is the coPol magnitude that contains system noise. The symbol $< \cdot >$ denotes an ensemble average. A 4×12 window in azimuth and slant range is applied to estimate $|\rho_n|$.

Noise effects on the coPol magnitude $|\rho_n|$ pertain to radar system characteristics and are independent of the scattering signal from sea ice. It is assumed that the noise between horizontal and vertical channels is uncorrelated and equal in amplitude (Nghiem et al., 1995b). Therefore, the de-noised coPol magnitude $|\rho|$ can be related to $|\rho_n|$ by (Nghiem et al., 1995b)

$$|\rho| = |\rho_n| \cdot \left(1 + \frac{1}{SNR}\right) \tag{2}$$

where $SNR = S(\mathrm{dB}) - N(\mathrm{dB})$ is the signal-to-noise ratio with S being the backscattering signal and N being the noise floor (i.e., the noise equivalent sigma zero (NESZ)). The TanDEM-X product contains a set of polynomial coefficients that describe the NESZ pattern for each polarization along the range direction (Eineder et al., 2008)

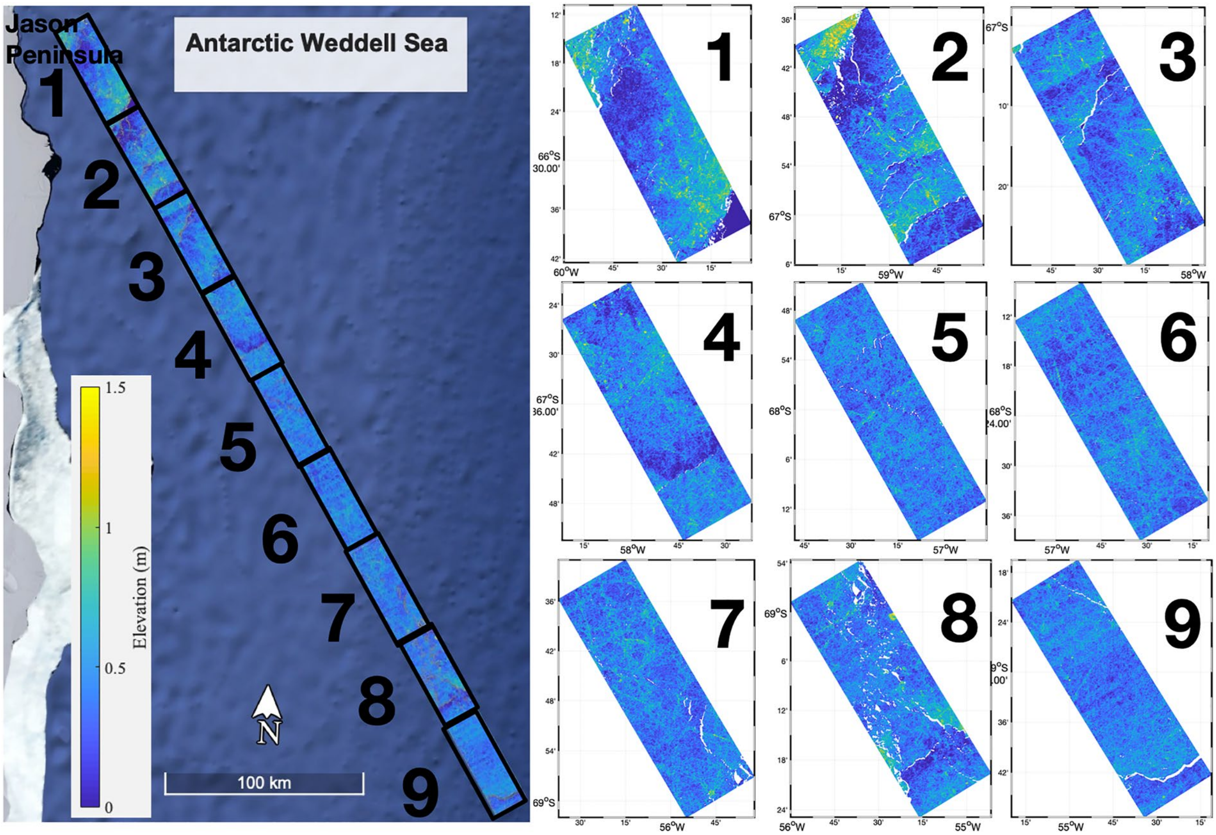

Figure 5. Averaged heights of InSAR phase center between HH and VV polarization.

for both the TanDEM-X (TDX) and TerraSAR-X (TSX) images. For each channel, the NESZ values along the range direction of Scene 1 are shown in Figure 6 as an example. For each TanDEM-X product, the noisy coPol magnitude $|\rho_n|$ can be calculated by Equation 1 and the averaged *SNR* in HH and VV polarization is estimated using the NESZ values. By substituting Equation 1 into Equation 2, the de-noised coPol magnitude $|\rho|$ is generated over the study area (shown in Figure 7) and will be used in the following analyses.

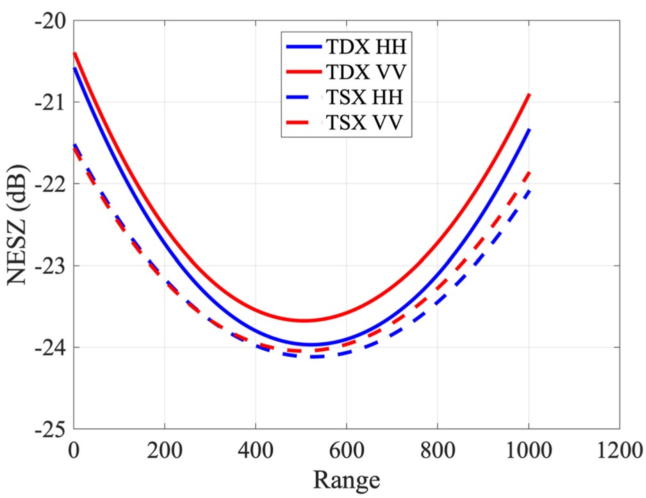

Figure 6. An example of noise equivalent sigma zero (NESZ) patterns for one TanDEM-X product (Scene 1).

Also, the phase balance between coPol channels should be checked to ensure that SAR data are well-calibrated. SAR data acquired over dense forest and water areas can be used to verify the phase balance between the radar horizontal and vertical channels. The phase $\angle\rho$ from forest areas is expected to be zero because forests likely have a random scattering behavior (Nghiem et al., 1993). The scattering from rough surface in water areas is expected to have a small value of $\angle\rho$ due to differences in the complex reflection coefficients for horizontal and vertical polarizations, especially at small incidence angles (Nghiem et al., 1993) where the transverse-electric and transverse-magnetic reflection coefficients are similar. From the analyses, TanDEM-X data are verified to have a good phase balance between the horizontal and vertical channels, as demonstrated by the near-zero $\angle\rho$ from both the in-scene water in the Weddell Sea where the mean $\angle\rho$ is $-1°$ with a standard deviation of 14°, and also from the off-scene forest data taken on the same date by the same acquisition mode where the phase is well balanced as the mean $\angle\rho$ is $-0.5°$ with a small standard deviation of 5°.

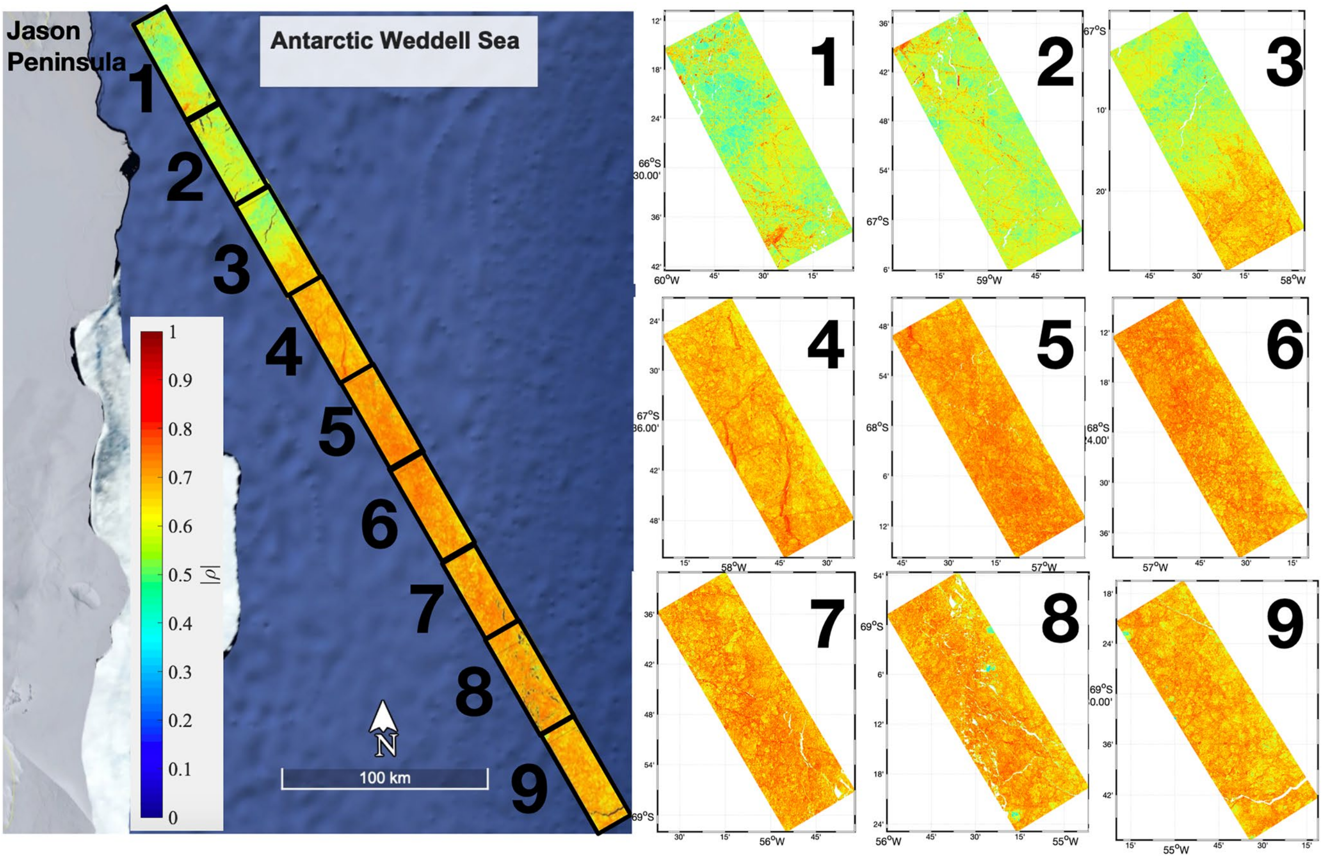

Figure 7. De-noised coPol magnitude |ρ|.

4. Sea Ice Classification

From the electromagnetic scattering physics based on the first principle of Maxwell's equations, the backscatter for the older, thicker, and rougher sea ice with snow cover is stronger than the younger, thinner, and smoother ones without snow (Nghiem et al., 1990, 1995a, 1993). From TanDEM-X observations over the Western Weddell Sea, backscattering patterns of the Antarctic snow-covered sea ice are presented in Figure 2, revealing a particular feature of sea ice backscattering signatures with higher values (>−10.8 dB) off the east coast of the Jason Peninsula and decreasing values away from the coast in a southeasterly direction. The highest backscatter intensity is observed in Scene 1, where the ice is deformed and ridged with snow accumulation seen from the DMS optical images.

For sea ice classification, backscatter data need to be processed to account for noise effects. The SAR-measured backscattering intensity σ_{measure} containing additive thermal noise can be denoted as

$$\sigma_{\text{measure}} = \langle (S_{\text{denoised}} + N) \times (S_{\text{denoised}} + N)^* \rangle \tag{3}$$

where S_{denoised} is the noise-subtracted backscattering amplitude, and N is the additive thermal noise. Considering S_{denoised} and N to be uncorrelated, the noise-subtracted backscattering intensity can be obtained from the following simple equation

$$\sigma_{\text{denoised}} = \sigma_{\text{measure}} - \text{NESZ} \tag{4}$$

where all terms are in linear domain. NESZ can be calculated for each polarization along the range direction (Eineder et al., 2008) for both the TDX and TSX images, shown in Figure 6 as an example in Section 3.4. For both HH and VV polarization, the noise-subtracted backscattering intensity can be generated using Equation 4 in

10.1029/2022EA002472

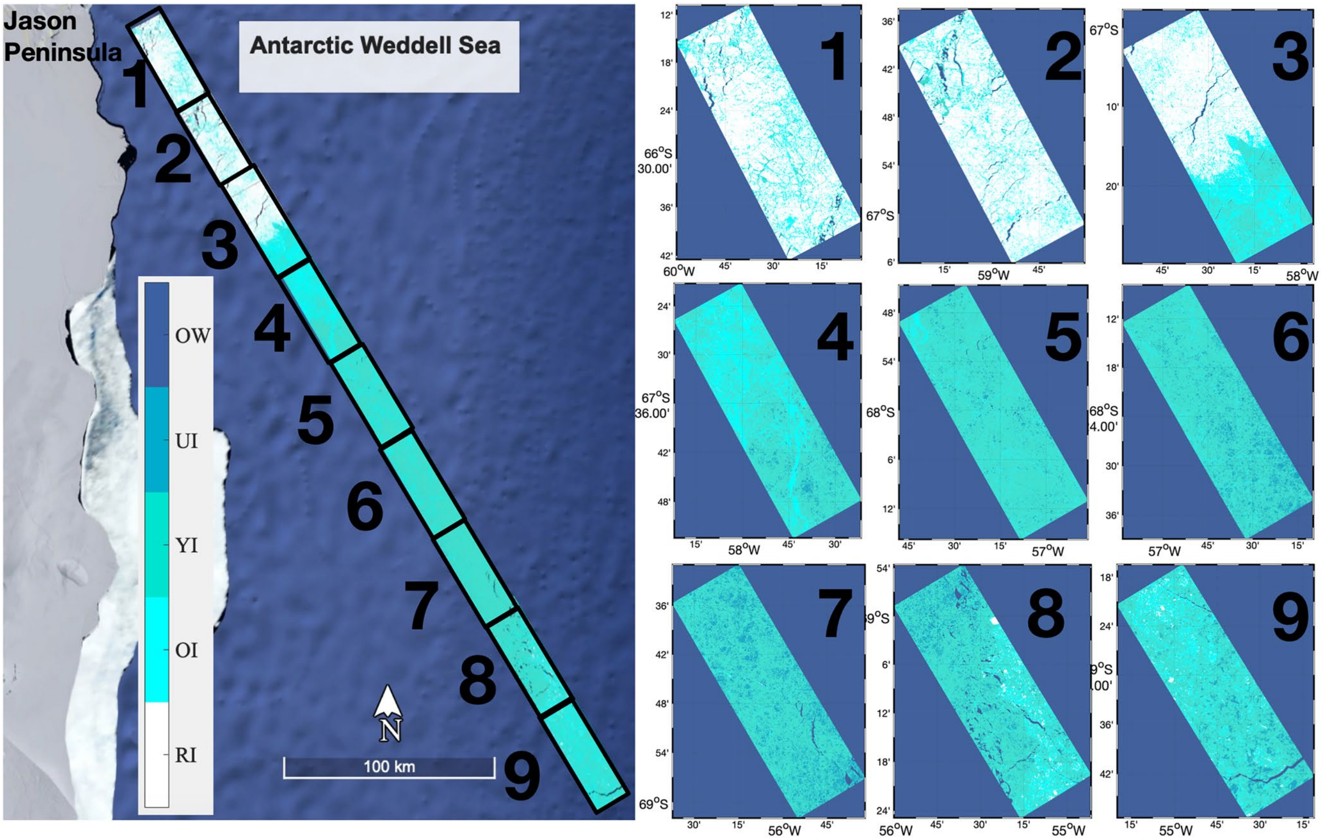

Figure 8. Synoptic classes of sea ice over the study area.

linear scale and then converted to decibel scale. Note that the backscattering differences between the two polarizations are marginal, and the averaged value (σ_{avg}) can reduce the system noise.

In Section 3.3, interferometric coherence below 0.3 is identified as open water (OW) area and has already been masked out. Statistic distribution of backscatter from sea ice has characteristics pertaining to different sea ice classes (Nghiem et al., 2016). Over the study area, SAR backscattering distribution has a double-peak pattern, where RI corresponds to the backscatter range under the high-backscatter peak, young ice (YI) is under to the low-backscatter peak, OI is between the two peaks, and new undeformed ice (UI) corresponds to the backscatter range lower than half value of the low-backscatter peak. Thereby, based on the averaged noise-subtracted backscattering intensity (σ_{avg}) between HH and VV polarizations, four sea ice classes over the study area are defined according to σ_{avg} as follows:

- Rough deformed ice (RI): $\sigma_{avg} > -10.8$ dB;
- Old ice (OI): -13.4 dB $< \sigma_{avg} \leq -10.8$ dB;
- Young ice (YI): -18 dB $< \sigma_{avg} \leq -13.4$ dB;
- Undeformed ice (UI): $\sigma_{avg} \leq -18$ dB;

A synoptic classification map is presented in Figure 8 and quantified in Table 1. Scenes 1 and 2 are mainly covered by OI and RI, where RI dominates ≥76% spatial area. A transition zone is observed in Scene 3, where the RI area reduces while the YI area enlarges. From Scenes 4 to 7, moving outward from the Jason peninsula, YI becomes the dominant class, and the coverage of UI grows. From Scene 8, with the higher latitude, sea ice becomes thicker and rougher again, while RI and especially OI areas start to expand in Scenes 8 and 9.

Table 1
Percentage of Different Sea Ice Classes Over the Study Area

Scene	RI	OI	YI	UI	OW
No. 1	**76%**	19%	4%	0%	1%
No. 2	**78%**	16%	3%	1%	2%
No. 3	**52%**	27%	19%	1%	1%
No. 4	0%	32%	**63%**	5%	0%
No. 5	0%	8%	**86%**	5%	1%
No. 6	0%	5%	**80%**	14%	1%
No. 7	0%	2%	**73%**	24%	1%
No. 8	2%	13%	**68%**	14%	3%
No. 9	2%	22%	**66%**	9%	1%

Note: The bold values show the highest percentage of sea ice classes.

10.1029/2022EA002472

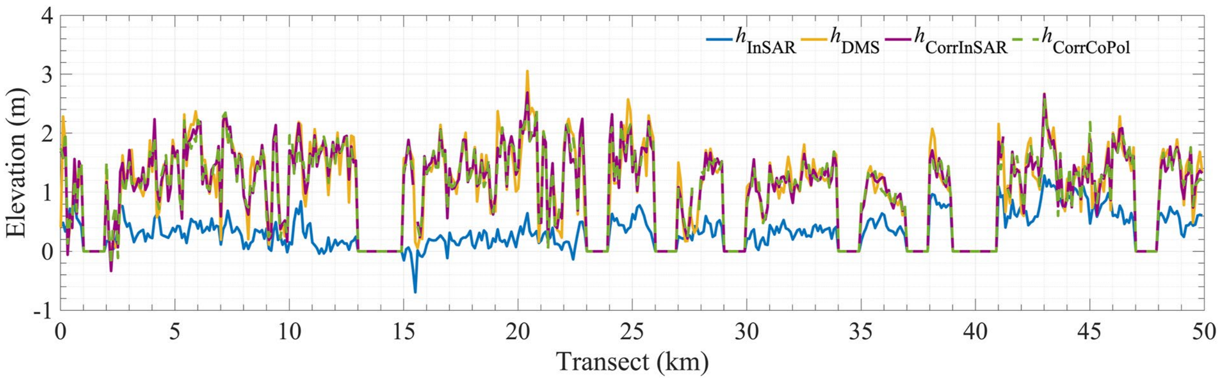

Figure 9. Sea ice elevation profiles along the 50 km transect from (interferometric synthetic aperture radar) InSAR, digital mapping system (DMS), and the proposed methods. The segments removed from the experiments due to misregistration are denoted as 0 m.

The above sea ice classes are identifiable based on the statistic distribution of the backscatter signal with higher values qualitatively corresponding to older, rougher, and thicker sea ice with higher DEM, in view of both volume and surface scattering physics (Nghiem et al., 1990, 1995a, 1995b, 2016). Per se, such nomenclatures of the sea ice classification are somewhat arbitrary as they do not have specific quantitative values of sea ice roughness associated with them. This is also the same issue with the World Meteorological Organization (WMO) nomenclatures of both Arctic and Antarctic sea ice (WMO, 2014), for which collocated and contemporaneous roughness and ice classification maps were not available to determine the roughness pertaining to each sea ice nomenclature. Once the sea ice DEM is obtained over a given sea ice class (see Sections 5 and 6), the nomenclature issue will be resolved as quantitative characterization of sea ice roughness can be associated specifically to the nominal sea ice class.

5. Elevation Retrieval for OI and RI

Following the InSAR processing described in Section 3.3, the phase center heights of sea ice over the study area are derived and shown in Figure 5. For the co-registered 50 km transect along the DMS flight track in Scene 1, the distinct discrepancy between the TanDEM-X elevation profile h_{InSAR} (blue line) and DMS elevation profile h_{DMS} (yellow line) as presented in Figure 9 becomes evident. The transect covering 5,000 pixels is too busy to be illustrated; therefore, only one pixel in every 10-pixel interval is selected and presented. This is only done for the visualization in Figure 9. Quantitatively, a comparison between h_{DMS} and h_{InSAR} reveals a RMS error (RMSE) along the transect of about 1.09 m. The large RMSE value suggests that the interferometric phase center for the derivation of the topographic height is not fully sufficient to retrieve an accurate DEM. In fact, the physical basis of the Antarctic sea ice (Nghiem et al., 2022) indicates the need to use coPol magnitude $|\rho|$, which contains ample information relevant to sea ice elevation, to generate sea ice DEM over OI and RI. In the next section, the relation between the de-noised $|\rho|$ from SAR images and the DMS-measured sea ice elevation is investigated and exploited for OI and RI DEM generation. Moreover, information from the single-pass interferometric data is also assessed and combined into the retrieval to enhance the accuracy of the sea ice DEM.

5.1. Decorrelation-to-Elevation Relationship

For the co-registered OI and RI samples, the de-noised coPol magnitude $|\rho|$ from SAR observations is calculated according to Equation 1 and Equation 2 and related to h_{DMS}. An inverse relation between $|\rho|$ and h_{DMS} is shown in Figure 10a, where $|\rho|$ ranges from 0.9 to 0.3 corresponding to h_{DMS} in the range from 0 to 3 m. For each co-registered segment, the negative trend is observed, and the absolute value of Pearson's r is given in Figure 11 (red bar). The observed inverse relation indicates that larger sea ice DEM corresponding to pronounced topography causes stronger depolarization and lower coPol magnitude $|\rho|$. This is consistent with the deformation process that OI and RI are undergoing, related to formation time and deformation with ridging and rafting features that consequently increase sea ice elevation. The inverse relation can be represented by a geophysical model function as

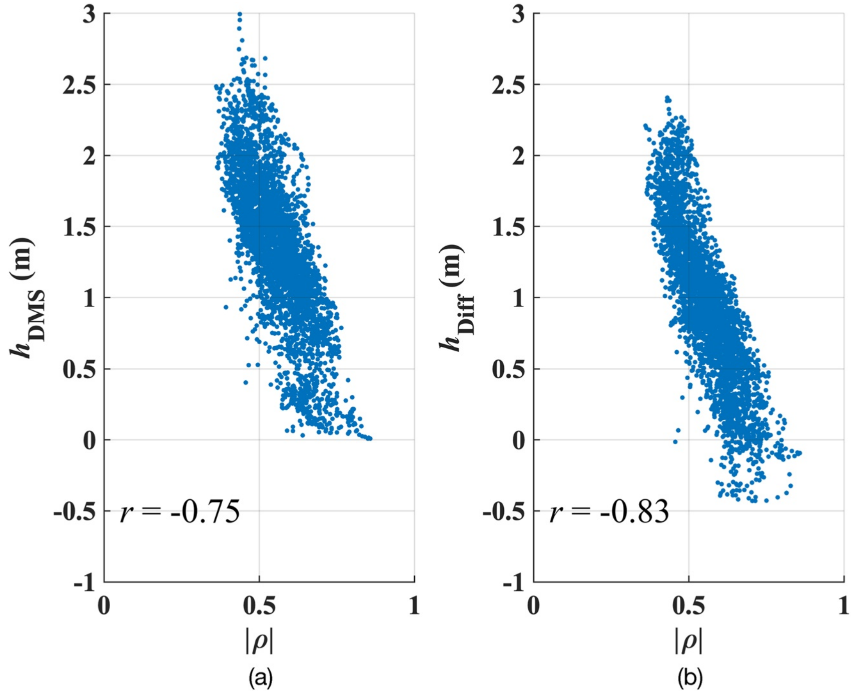

Figure 10. Inverse relationships between the $|\rho|$ and h_{DMS} (left) or h_{Diff} (right) over the co-registered segments.

$$h_{\mathrm{CorrCoPol}} = k_1 \cdot |\rho| + b_1 \tag{5}$$

where $h_{\mathrm{CorrCoPol}}$ is the model-derived elevation, and k_1 and b_1 are coefficients estimated by a least-square method based on the measured h_{DMS} and $|\rho|$. Linear regression is conducted to estimate k_1 and b_1 for each segment, respectively. For all co-registered segments, the mean and standard deviation of k_1 and b_1 are -5.09 ± 1.54 and 4.20 ± 0.89, respectively.

The physical principles of the inverse relation between $|\rho|$ and sea ice DEM has been proven by Nghiem et al. (2022). As a result of wind and wave dynamic in the Western Weddell Sea (Nghiem et al., 2016), sea ice becomes ridged, thickened, and elevated, leading to desalination through processes such as gravity drainage (Gow et al., 1987; Weeks & Ackley, 1982). As older sea ice is formed earlier and has a longer time to undergo deformation processes, the surface is more elevated where more desalination occurs. Also, thick sea ice can undergo severe ridging due to strong storm forcing in the Antarctic (Massom & Stammerjohn, 2010). These inter-related processes suggest a potential relation between sea ice DEM and desalination for old, rough, and deformed sea ice. By setting properties of snow-covered sea ice pertaining to Antarctic sea ice conditions, $|\rho|$ is simulated from

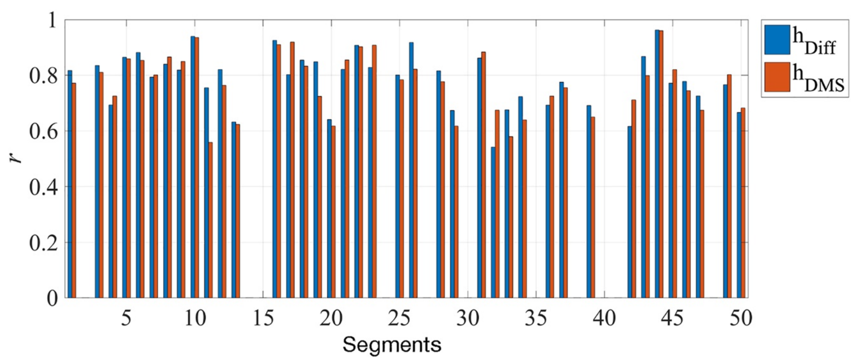

Figure 11. Absolute value of Pearson's r between $|\rho|$ and h_{DMS} (red) and h_{Diff} (blue) for the 39 co-registered segments used in the experiments. The x-axis indicates the serial number of the segments. The 11 misregistered segments are excluded.

10.1029/2022EA002472

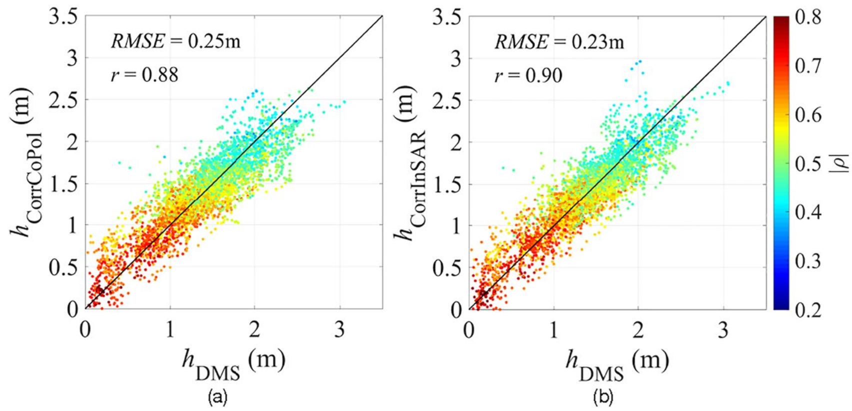

Figure 12. Correlation between (a) h_{DMS} and CorrCoPol DEM ($h_{\mathrm{CorrCoPol}}$), and (b) h_{DMS} and CorrInSAR DEM ($h_{\mathrm{CorrInSAR}}$).

the model and shows an inverse relation to sea ice elevation (Nghiem et al., 2022). The electromagnetic model simulation showing a linear relation as $h_{\mathrm{CorrCoPol}} = -5.28|\rho| + 4.31$ (Nghiem et al., 2022) is closely consistent with the geophysical model function $h_{\mathrm{CorrCoPol}} = -5.09|\rho| + 4.20$ derived from the co-registered segments from OTASC measurements. Fundamentally supported on the foundation of the first-principle physics (Nghiem et al., 2022) and directly derived from field data in the Antarctic, the geophysical model function $h_{\mathrm{CorrCoPol}} = -5.09|\rho| + 4.20$ can thus be used to reconstruct a sea ice DEM over the study area.

Over the co-registered transect, the coPol-corrected (Corr CoPol) elevation $h_{\mathrm{CorrCoPol}}$ derived from Equation 5 is shown (green dash line) in Figure 9, where the plot illustrates that the profile of $h_{\mathrm{CorrCoPol}}$ can effectively capture the profile of h_{DMS}. A quantitative comparison is presented in Figure 12a, where the RMSE and the Pearson's r between $h_{\mathrm{CorrCoPol}}$ and h_{DMS} are 0.25 m and 0.88, respectively. Compared to the original InSAR-derived elevation (RMSE = 1.09 m), the pronounced improvement demonstrates the effectiveness of applying $|\rho|$ to generate sea ice DEM. The geophysical model function Equation 5 with the mean value of $k_1 = -5.09$ and $b_1 = 4.20$ is employed to obtain sea ice DEM for OI and RI over the study area, illustrated in Figure 13. Since the above retrieval method is only applicable to OI and RI, the pixels of YI, UI, and OW area are set to be transparent in Figure 13. An animation of a simulated fly over the estimated DEM map (i.e., $h_{\mathrm{CorrCoPol}}$) of the OI and RI in Scenes 1–3 is given in the Supporting Information.

5.2. Additional Topographic Information From Interferometry

The elevation difference h_{Diff} between h_{DMS} and h_{InSAR} is defined as

$$h_{\mathrm{Diff}} = h_{\mathrm{DMS}} - h_{\mathrm{InSAR}} \tag{6}$$

An inverse relationship between h_{Diff} and $|\rho|$ is observed in Figure 10b. The absolute values of Pearson's r for the 39 co-registered segments are presented in Figure 11 (blue bar). Compared to the correlation between the h_{DMS} and $|\rho|$ shown in red, the correlation between h_{Diff} and $|\rho|$ yields a larger absolute value in most cases, indicating slightly improved correlations between $|\rho|$ and h_{Diff} than h_{DMS}. The linear function is also utilized to describe the observed inverse relation

$$\hat{h}_{\mathrm{Diff}} = k_2 \cdot |\rho| + b_2 \tag{7}$$

where $\hat{h}_{\mathrm{Diff}}$ is the elevation difference derived from the function, and k_2 and b_2 are estimated by the least-square method from each segment. For the co-registered segments, the mean and standard deviation of k_2 and b_2 are -4.87 ± 1.54 and 3.65 ± 0.84, respectively. The InSAR-corrected (CorrInSAR) elevation $h_{\mathrm{corrInSAR}}$ is given by

$$h_{\mathrm{CorrInSAR}} = h_{\mathrm{InSAR}} + \hat{h}_{\mathrm{Diff}} \tag{8}$$

The $h_{\mathrm{CorrInSAR}}$ along the co-registered transect is shown (violet line) in Figure 9, where the profile of $h_{\mathrm{CorrInSAR}}$ agrees well with the h_{DMS}. A quantitative comparison is illustrated in Figure 12b for the co-registered segments. The RMSE and the Pearson's r between $h_{\mathrm{CorrInSAR}}$ and h_{DMS} are 0.23 m and 0.90, respectively, showing a higher

10.1029/2022EA002472

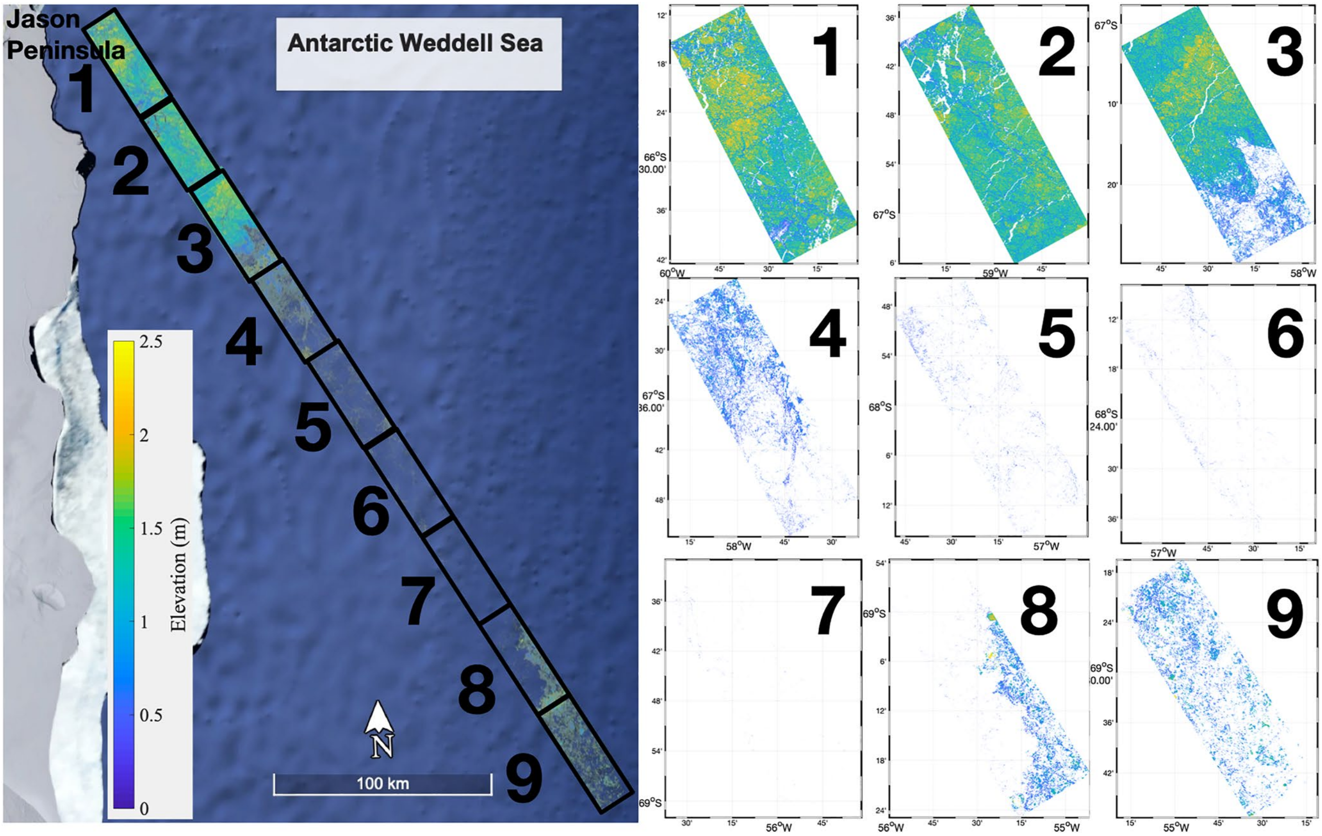

Figure 13. CorrCoPol digital elevation model (DEM) ($h_{\mathrm{CorrCoPol}}$) for old ice (OI) and rough deformed ice (RI) in the Western Weddell Sea. The pixels of young ice (YI), undeformed ice (UI), and open water (OW) area are set to be transparent.

accuracy than the retrieval that only uses coPol magnitude. Note that DMS DEM measurements include an inherent uncertainty of 0.2 m (Dotson & Arvesen, 2012, updated 2014).

The results suggest that in addition to $|\rho|$, which carries crucial information on sea ice elevation, interferometric information brings supplementary knowledge to help improve the accuracy of sea ice DEM. Therefore, combining the polarimetric signature with interferometric information represents an optimal method for sea ice DEM generation. For OI and RI in the study area, $h_{\mathrm{CorrInSAR}}$ is estimated using Equation 7 and Equation 8 with the mean value of $k_2 = -4.87$ and $b_2 = 3.65$, and is presented in Figure 14.

Whether the relation between $|\rho|$ and sea ice elevation may or may not exist for different regions and seasons of sea ice needs to be investigated as the physical structures and properties of sea ice are different in different regions and seasons. For Arctic sea ice, the approximate inverse relation between $|\rho|$ and the cross-polarization ratio was observed over multi-year sea ice but not over first-year sea ice (Nghiem et al., 1993). With more coincident data sets of sea ice elevations, polarimetric-interferometry SAR imagery, as well as environmental and sea-ice parameters in the future, the model capabilities can be explored to test the applicability for monitoring Arctic sea ice elevation, Great Lakes ice height, lake-ice level across the cold landscape, or other geophysical parameters in different environments of the Earth.

6. Characterization of Sea Ice Topography

6.1. Generation of Sea Ice DEM 3D Patterns

Sea ice DEM can be statistically characterized by parameters such as roughness of sea ice, auto-correlation length, and orientation angle, providing the basis for quantitative analyses of sea ice characteristics in 3D with respect to the corresponding geophysical and environmental conditions in the Antarctic. Due to the dominant

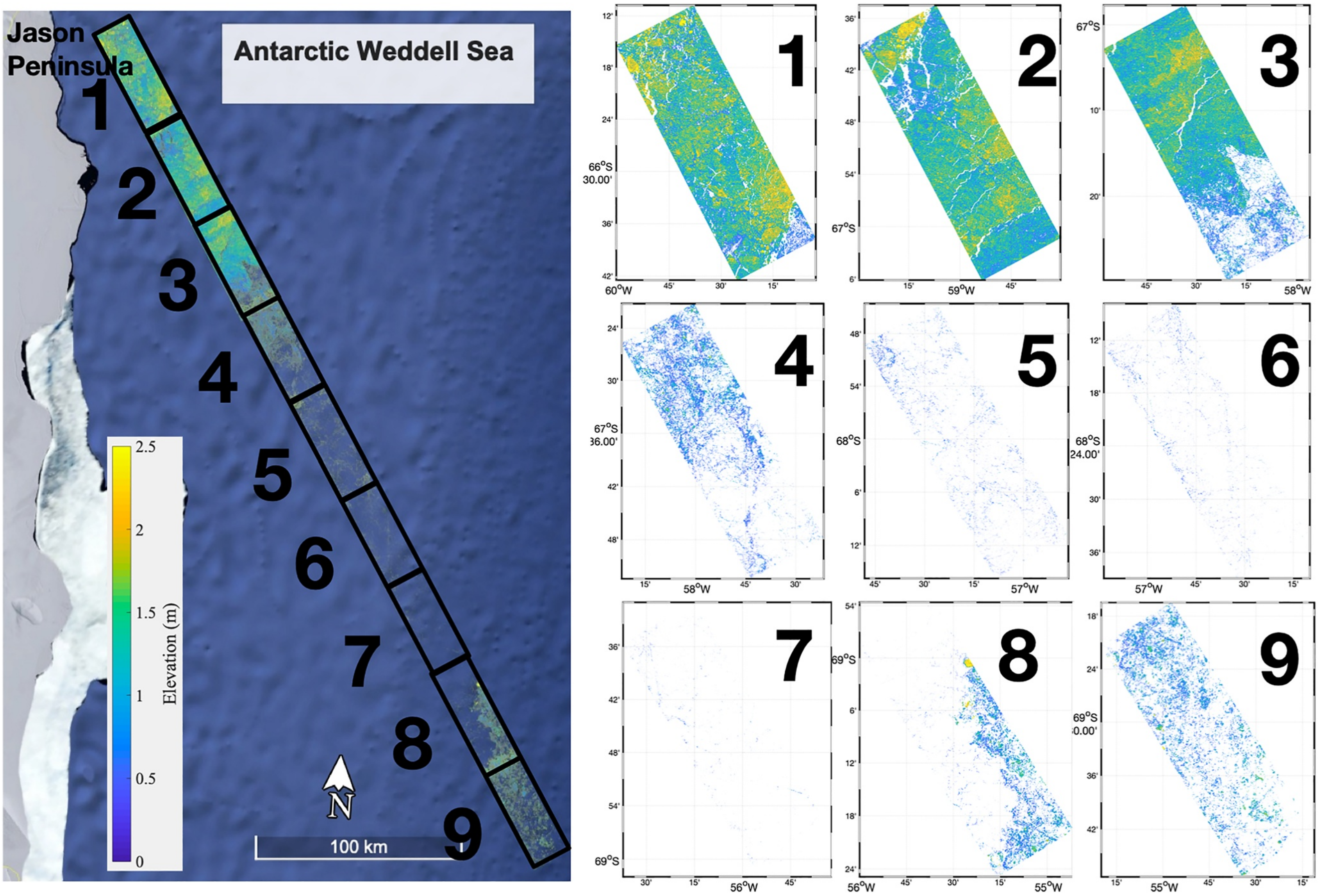

Figure 14. CorrInSAR digital elevation model (DEM) ($h_{\mathrm{CorrInSAR}}$) for old ice (OI) and rough deformed ice (RI) in the Western Weddell Sea. The pixels of young ice (YI), undeformed ice (UI), and open water (OW) area are set to be transparent.

coverage of OI and RI over Scenes 1–3 (see Figure 14), these three scenes are selected for the analyses in this section.

Sea ice roughness can be measured in terms of the RMS height, which is defined as

$$h_{\mathrm{RMS}} = \sqrt{\mathbb{E}\left(\left(h_{\mathrm{CorrInSAR}} - \hat{h}_{\mathrm{CorrInSAR}}\right)^2\right)} \tag{9}$$

where $h_{\mathrm{CorrInSAR}}$ is the sea ice elevation of each pixel in the subset (Figure 15b), and $\hat{h}_{\mathrm{CorrInSAR}}$ is the average elevation in the subset. As illustrated in Figure 15a, the SAR scene is partitioned into subsets with $N \times N$ spatial resolution for each subset. Here N is set to be 100 m, and h_{RMS} is derived from Equation 9 for each subset.

A comparison between the h_{RMS} derived from the CorrInSAR DEM and from the DMS DEM over the co-registered transect is given in Figure 16, where the Pearson's $r = 0.71$ and RMSE $= 0.1$ m. It confirms that the accuracy of h_{RMS} from CorrInSAR DEM is nearly as precise as the one from DMS DEM. SAR-retrieved h_{RMS} over Scenes 1–3 is visualized in Figure 17a and quantified in Figure 17b, where the roughness ranges from 0 to 1 m across a 19×150 km area covered by OI and RI. The average and standard deviation of roughness for OI and RI are similar, around 0.23 ± 0.10 m and 0.25 ± 0.11 m, respectively. The probability density function (PDF) of the observed h_{RMS} can be fitted by a three-parameter gamma distribution (Cohen & Norgaard, 1977)

$$f(x) = \frac{1}{\Gamma(k)\theta^k}(x-\mu)^{k-1} e^{-\frac{x-\mu}{\theta}} \qquad \mu < x < \infty, k > 0, \theta > 0 \tag{10}$$

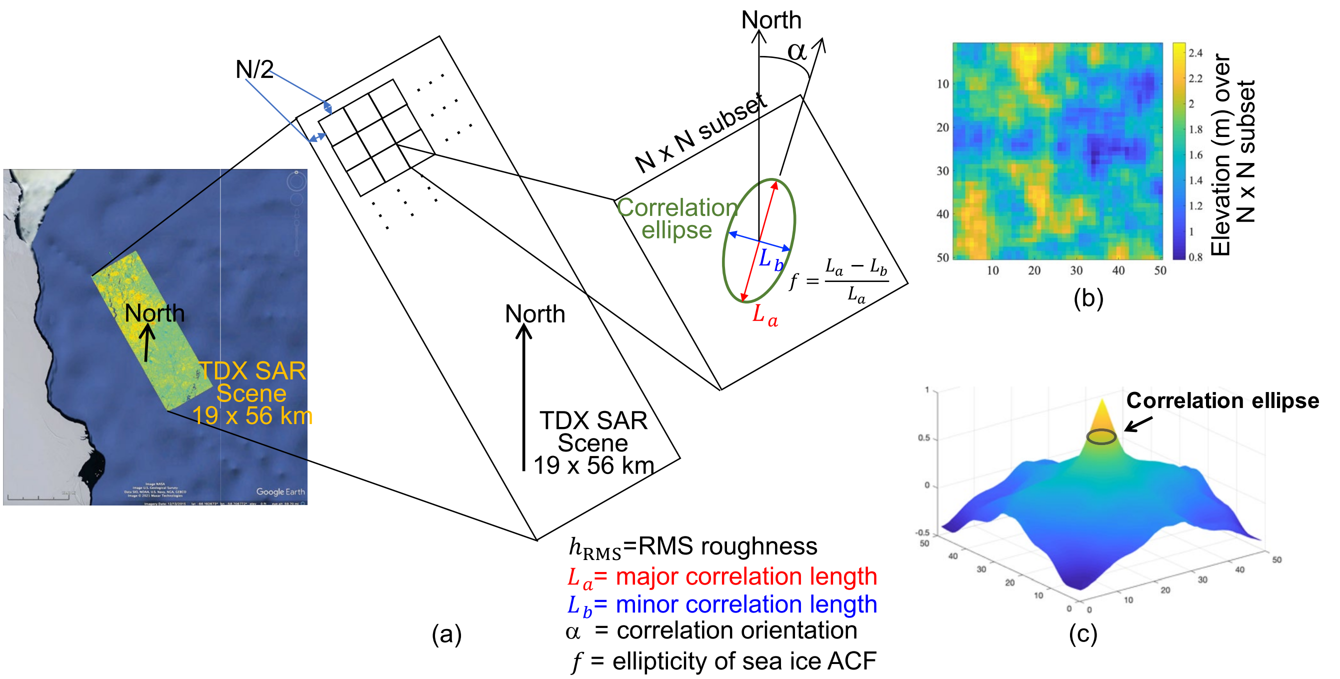

Figure 15. (a) Definition of parameters for sea ice digital elevation model (DEM) 3D characterization. (b) An example of sea ice CorrInSAR DEM over the $N \times N$ subset. (c) Auto-correlation function (ACF) analysis over the $N \times N$ subset.

where Γ(.) is the gamma function, k and θ are the shape and scale parameter, respectively, and μ is the location parameter of the gamma random variable. The fitted PDFs of gamma distributions are calculated by matching the mean, variance, and skewness given the observed h_{RMS} with a cutoff set at 0.5 m, where >95% samples lie in the range of $h_{\mathrm{RMS}} < 0.5$ m. As shown in Figure 17b, for both RI and OI, the three-parameter gamma distributions suggest good descriptions with the observed roughness.

The gamma distribution usually represents processes occurring toward a termination event such as sea ice evolution until the ice season end date (Nghiem et al., 2014). In the case of this study, sea ice becomes more roughened, thickened, and elevated as the ice becomes older toward the end of the sea ice season in the Weddell Sea. Figure 17b notably shows that the RI has the largest skewness as the PDF becomes asymmetric toward the high range of the thick and elevated sea ice compared to that of the OI with weaker backscatter corresponding to lower roughness.

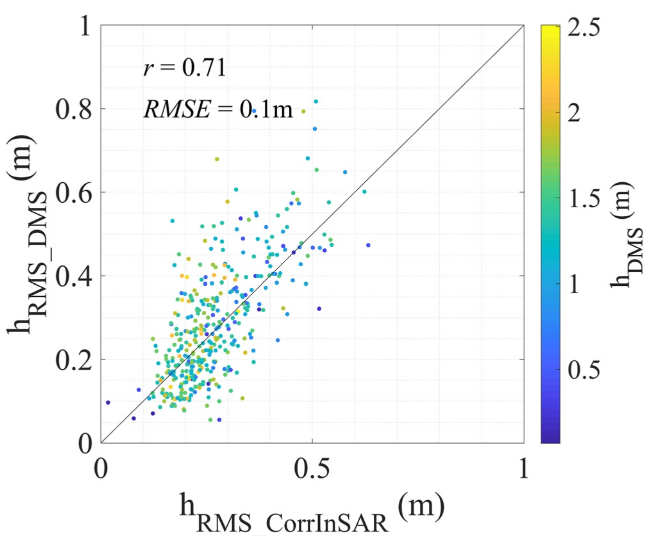

Figure 16. Comparison of the h_{RMS} derived from the CorrInSAR digital elevation model (DEM) and digital mapping system (DMS) DEM over the co-registered transect.

The auto-correlation length is a function describing the contour of the 2D auto-correlation function (ACF) with a normalized correlation of e^{-1}, shown in Figure 15c. The e^{-1} correlation contour is non-circular in general and can be characterized with an ellipse, and four ACF parameters are extracted from the ellipse. The major (minor) correlation length L_a (L_b) corresponds to the major (minor) axis of the correlation ellipse. The ellipticity is defined as $f = (L_a - L_b)/L_a$. The orientation angle α describes the direction of the major axis to the north direction (see Figure 15a). The four ACF parameters can be estimated for each subset with $N \times N$ spatial resolution, where N = 500 m. Note that N = 500 m is a trade-off value between the number of samples and spatial resolution. For some subsets, the contour of ACF cannot be well represented by an ellipse when N < 500 m due to the deficient number of samples.

Figure 18 shows the distributions (in histograms) of α, e, L_a, and L_b, each of which is calculated for Scenes 1–3. In Figure 18a, the orientation angle α involves the similar shape of distribution with close values of the mean

10.1029/2022EA002472

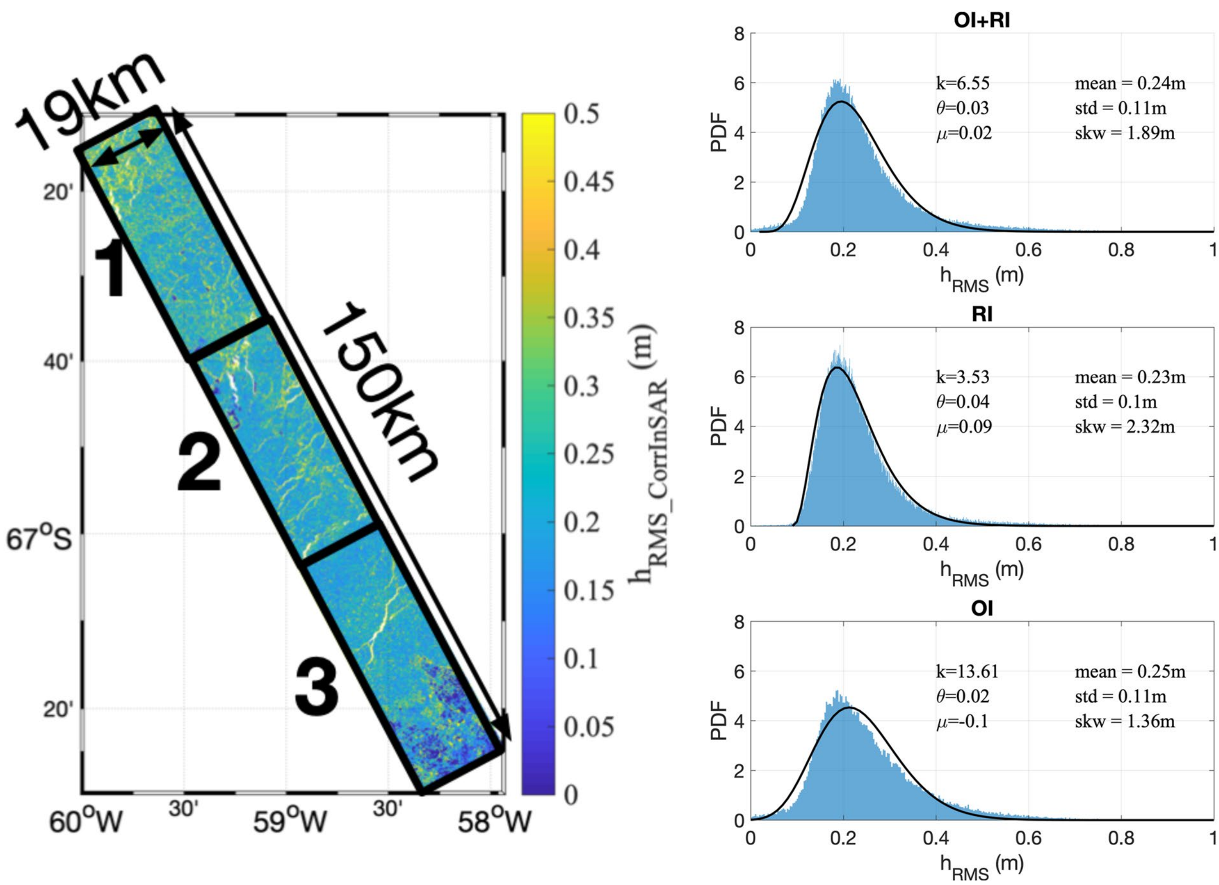

Figure 17. (a) h_{RMS} derived from the CorrInSAR digital elevation model (DEM) for Scenes 1–3. (b) Histogram of h_{RMS} derived from the CorrInSAR DEM for Scenes 1–3. The mean, standard deviation (i.e., std), and skewness (i.e., skw) are calculated given all the observed h_{RMS}. The black lines denote the three-parameter gamma distributions with k, θ, and μ estimated from samples with $h_{\mathrm{RMS}} < 0.5$ m.

and standard deviation in Scenes 1–3, and so do the other three ACF parameters e, L_a, and L_b as shown in Figures 18b–18d. This statistical similarity between the same parameter among different scenes suggests that the sea ice 3D structure over the areal scale of ∼19 × 150 km was formed under similar regional atmospheric driver (e.g., katabatic winds) and/or oceanic forcing (e.g., ocean circulations) in this particular sector of the Western Weddell Sea.

6.2. Sea Ice DEM 3D Patterns Related to Bathymetry

Nghiem et al. (2016) found that the patterns of Antarctic sea ice classes are consistent with bathymetry over large scales (100–1,000 km); however, 3D sea ice patterns versus bathymetry at smaller scales (1–100 km) remain to be examined. In this subsection, the patterns of sea ice DEM (i.e., $h_{\mathrm{CorrInSAR}}$) related to bathymetry are analyzed in terms of bathymetric depth and aspect angle. The General Bathymetric Chart of the Oceans (GEBCO) provides gridded bathymetry data that are available for public use and have a global coverage including the Antarctic Ocean (GEBCO Compilation Group, 2020). Figure 19a illustrates the retrieved sea ice DEM ($h_{\mathrm{CorrInSAR}}$) superimposed on the bathymetry for Scenes 1–3. Since the bathymetry data have a coarser resolution compared to the retrieved sea ice DEM, the average $h_{\mathrm{CorrInSAR}}$ is calculated in each pixel of GEBCO bathymetry data.

The Pearson's r between the averaged $h_{\mathrm{CorrInSAR}}$ and bathymetric depth is only 0.2. The low value of r indicates that the small-scale bathymetry may not exert uniform impacts on the elevation height of OI and RI in Scenes 1–3 over the bathymetry range from 300 to 800 m. The histogram shown in Figure 19b represents the number of data samples in each bin, which is 0.1 m in sea ice elevation and 20 m in bathymetric depth. It reveals that high elevations of OI and RI from 0.8 to 1.7 m with a pronounced double-peak pattern can occur over both a shallower range of 300–550 m depth, referred to as Sector 1 in Figure 19b and with a less occurrence pattern over a deeper

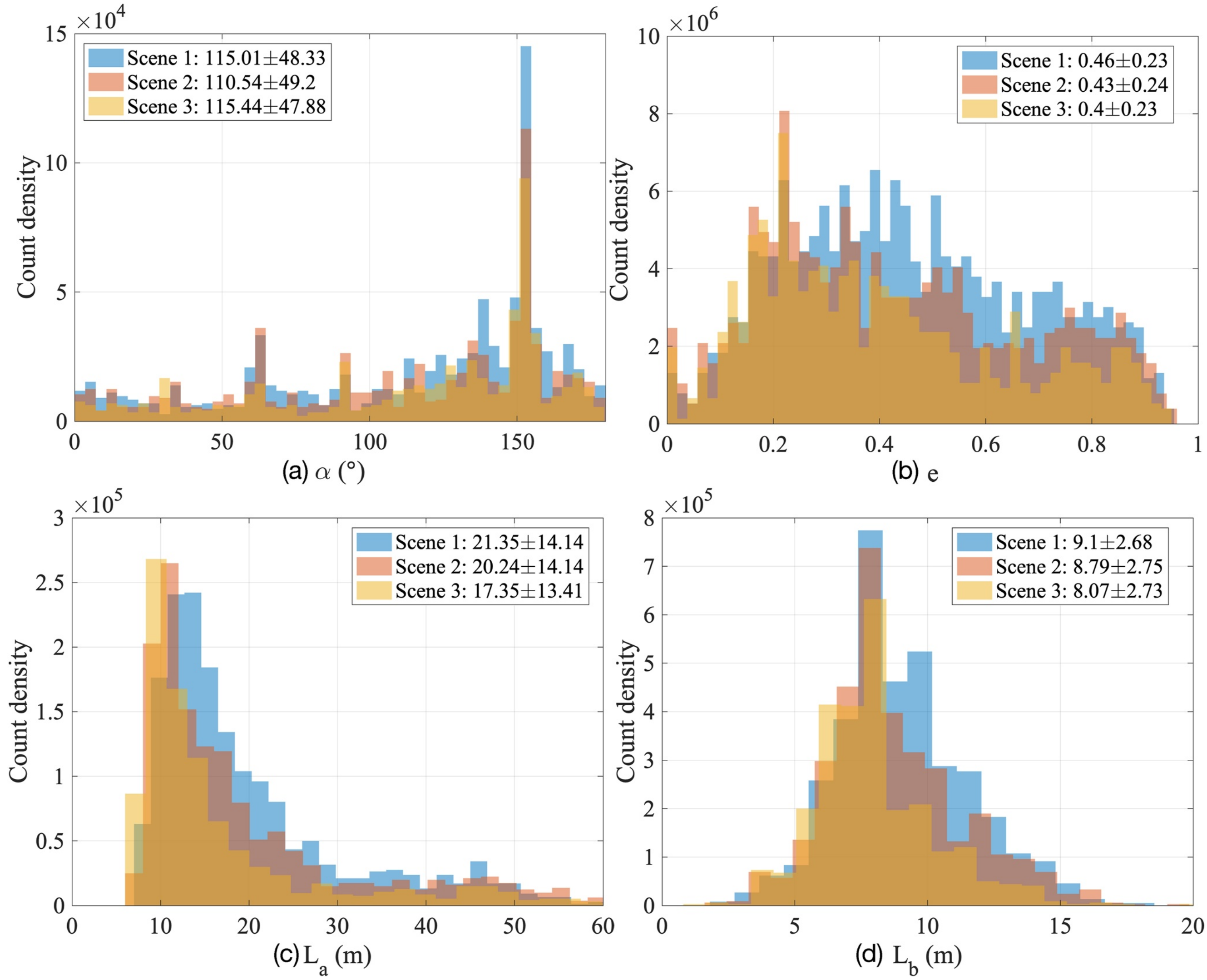

Figure 18. The histograms of (a) auto-correlation function (ACF) orientation angle α, (b) ellipticity f, (c) long axis L_a, and (d) short axis L_b derived from the CorrInSAR digital elevation model (DEM) for Scenes 1–3. The mean value ± standard deviation of each parameter for each scene is given on the subfigures.

range of 550–800 m depth, marked as Sector 2, while low elevations of OI and RI from 0.3 to 0.6 m can cluster over the mid-range of the bathymetry from 520 to 640 m depth, denoted as Sector 3. These complex patterns of sea ice DEM over various depths of the seafloor are consistent with a low Pearson's $r = 0.2$; however, the sea ice DEM is not randomly distributed and shows pronounced patterns over different ranges of the seafloor depth. These observations suggest a possible hypothesis that seafloor structures may exert confounding effects on the formation of the sea ice DEM in 3D, for which a future field campaign can be carefully developed with in-situ measurements of key oceanic parameters such as Conductivity-Temperature-Depth (CTD) profiling together with multi-beam sonar scans along multiple hydrographic sections.

Figure 18a reveals that the orientation angle α clusters around 153°, which may hypothetically depend on the sea bathymetry that guides sea currents in the subsurface marine environment. To examine this hypothesis, we define the bathymetric aspect angle ξ as the direction of the bathymetric slope relative to the north. Note that ξ ranges from 0° to 360°, while α is from 0° to 180° as it does not matter whether α is upslope or downslope with respect to ξ by definition.

As illustrated in Figure 20, consider a seafloor feature such as a trough or a channel that guides a sea current in parallel along the channel direction. In this ideal hypothetical case, the current compresses sea ice to form ridges

10.1029/2022EA002472

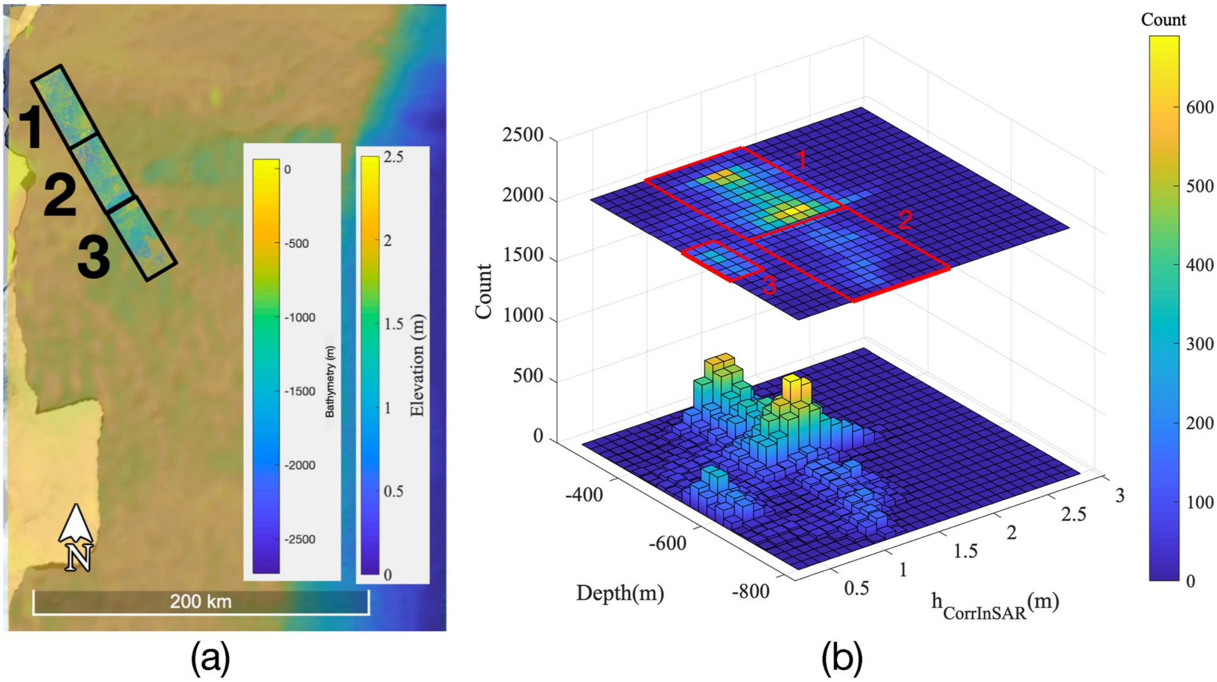

Figure 19. (a) CorrInSAR digital elevation model (DEM) ($h_{\mathrm{CorrInSAR}}$) is superimposed on the bathymetric depth map for Scenes 1–3. (b) 2D-histogram of $h_{\mathrm{CorrInSAR}}$ and bathymetric depth for old ice (OI) and rough deformed ice (RI) from Scenes 1–3.

that preferentially align in the direction perpendicular to the sea current direction. In this case, the ACF orientation is perpendicular to both the current direction and the isobath contour and is therefore parallel to the aspect direction and the gradient line, which is defined as the line perpendicular to the isobath contour, so that α forms an angle of 0° or 180° with respect to the aspect angle.

Figure 21 shows that the gradient lines generally align along the north-south direction and indeed indicate that α is parallel to the gradient line in many locations. However, a discrepancy of 27° (=180° − 153°) is observed from the real data in the histogram of the ACF orientation angle α, as shown in Figure 18a. Thus, α may possibly

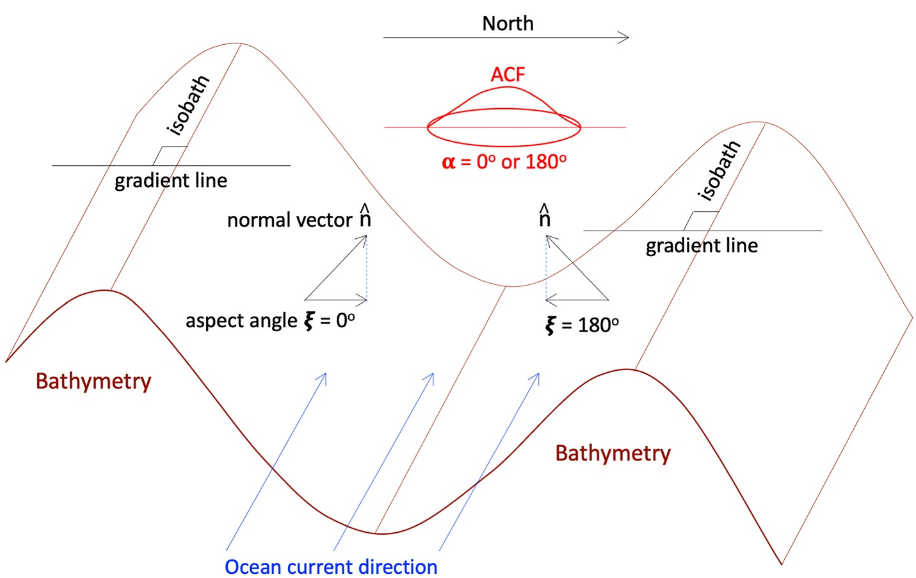

Figure 20. An ideal case of bathymetry guiding sea current and thereby exerting effects on auto-correlation function (ACF) orientation angle α alignment with the aspect angle ξ.

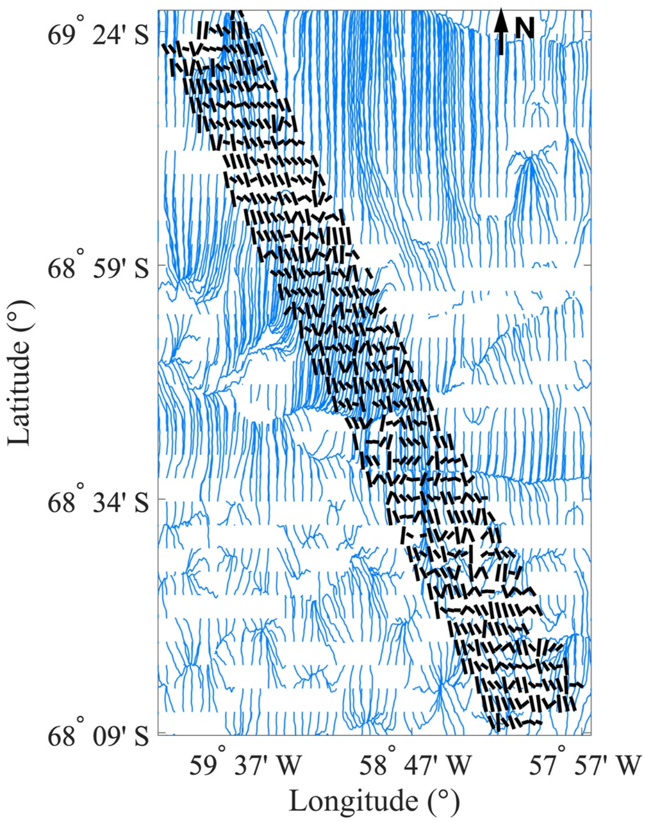

Figure 21. The map of orientation angle α overlaid on the gradient lines for Scenes 1–3.

deviate away from the ideal channel-guidance hypothesis at locations where the sea current may not be strongly guided preferentially along with the directional bathymetric features, or the seafloor may not have a pronounced directional features at such locations, or other forcing factors such as winds may partially contribute to the sea ice dynamics. The discrepancy can also be caused by uncertainty in the ACF estimation of α, or by biases from the regression fitting of grid bathymetry data (Smith & Sandwell, 2004). Note that our knowledge of bathymetry in the Southern Ocean is very limited (Millan et al., 2020), and the GEBCO bathymetry may have some uncertainty as some recorded seal dive data show deeper sea floor than that provided by GEBCO (Harcourt et al., 2021). The results highlight the requirements of in-situ measurements (such as CTD, ocean current, wind speed and direction, high-resolution sonar scans, etc.) in future sea ice scientific experiments to robustly examine processes contributing to the anisotropic formation of sea ice DEM with a preferential alignment.

7. Summary and Conclusions

This paper has derived a sea ice DEM for the two ice types (i.e., OI and RI) and provided 3D topographic characterization over a 19 × 450 km sector in the Western Weddell Sea using the coordinated campaign between TanDEM-X SAR and DMS optical data. For the snow-covered OI and RI, the sea ice elevation measured from DMS photographic technique was observed to be inversely correlated to coPol magnitude $|\rho|$ from SAR imagery, which is consistent with theoretical predictions. The experimental observations further concluded that $|\rho|$ carries significant information on sea ice DEM for OI and RI and can combine with interferometry to achieve an accurate DEM from single-pass InSAR data. The verification using the co-registered segments suggests a high retrieval accuracy with RMSE being 0.23 m.

Sea ice elevation retrieved from SAR data over large ground swaths is crucial for investigating sea ice formation and evolution processes within the context and constraints of geophysical and environmental conditions. A quantitative description of the sea ice DEM 3D pattern in terms of sea ice roughness and auto-correlation parameters, derived from the SAR-retrieved DEM, was presented and analyzed along the sector covered by OI and RI. The sea surface roughness was estimated with a mean of ∼0.24 ± 0.11 m where a range from 0 to 1 m was observed. The roughness statistical distributions resemble the characteristics of the gamma distribution for both OI and RI, while RI exhibits larger skewness than OI. The similar statistical distributions of roughness and auto-correlation parameters across the three scenarios reflect the similar sea ice DEM 3D pattern over the scale of ∼19 × 150 km in this sector of the Weddell Sea.

Based on the sea ice DEM 3D pattern, the clusters of bathymetric depth for various ranges of sea ice elevations were discussed. On higher sea ice elevations from 0.8 to 1.7 m, clusters over both shallower bathymetry ranges (300–550 m) and deeper range (550–800 m) depths were observed, while lower elevations of sea ice from 0.3 to 0.6 m mainly occur over the mid-range (520–640 m) depths of the bathymetry. Moreover, the orientation angle α clustering at 153° was hypothesized to be aligned preferentially along the bathymetric gradient lines, especially at the locations where the direction of sea current is guided by the seafloor features. In contrast to past geophysical studies based on 2D characterizations of sea ice such as sea ice concentration (De Veaux et al., 1993; Mack et al., 2013) and sea ice velocity from 2D images (Geiger & Drinkwater, 2005; Hutchings et al., 2012), the results presented here are the first findings of the quantitative characterization of high-resolution sea ice DEM in 3D over a large region in the Weddell Sea. These 3D observations of sea ice are valuable to pose new science hypotheses and to guide future field campaigns in order to advance the understanding of interactions among sea ice, air, ocean, and seafloor.

The spaceborne single-pass InSAR acquisition, such as the current TanDEM-X, provides optimal conditions for retrieving sea ice topography over extensive spatial coverage. With more single-pass or multi-static InSAR acquisitions in the future, for example, the European Space Agency mission Harmony which is envisaged to comprise two identical satellites flying in convoy with the Sentinel-1, a long-term and large spatial measurement of sea ice topography will be possible. Monitoring sea-ice topographic characteristics would be essential to further understand the geophysical processes of sea ice and to assess the impacts of the altered sea ice cover in a changing climate.

Regarding practical application such as the safety of maritime operations in ice-covered waters, which is a primary aim of the International Ice Charting Working Group (IICWG, 2021), the capability to associate quantitative characteristics of sea ice DEM to different sea ice classes (Section 6) can provide useful information relevant to navigation hazards in areas where large ridges are likely to be encountered (such as RI). With multiple satellite SAR data sets at X band (e.g., TSX/TDX, COSMO-SkyMed, and the future LOTUSat Missions), at C band (e.g., Sentinel-1, RADARSAT Constellation), and at L and S bands (e.g., SAOCOM, and the upcoming NISAR Mission), mapping products of sea ice classes can be operationally and synergistically obtainable from the international SAR missions with frequent and extensive coverage without requiring costly SAR full-polarimetric and InSAR capabilities.

Data Availability Statement

TanDEM-X data can be obtained from the German Aerospace Center (DLR) with scientific proposal and downloaded from https://eoweb.dlr.de (DLR, 2022). DMS data can be obtained from the National Snow and Ice Data Center and downloaded from https://nsidc.org/data/icebridge (NSIDC, 2022).

Acknowledgments

The research carried out at ETH Zürich was supported by the data obtained from OTASC efforts with participations and collaborations by the German Aerospace Center in Germany (in particular the strong support of Prof. Alberto Moreira for OTASC), NASA Goddard Space Flight Center in USA, University of Texas at San Antonio in USA, Woods Hole Oceanographic Institution in USA, Columbia University in USA, University of Canterbury in New Zealand, York University in Canada, the Alfred Wegener Institute in Germany, the U.S. National Ice Center in USA, University of Washington in USA, and University of Minnesota in USA. The research carried out at the Jet Propulsion Laboratory (JPL), California Institute of Technology, was supported by the NASA Cryosphere Science Program. We thank Shanghai Jiao Tong University in China for the promotion of Postdoctoral Program. Specifically for the English proofreading of this paper, we thank Mr. David Lee and Ms. Allyson Beatrice, who are professional Technical Writer Editor at JPL.

References

Abdalati, W., Zwally, H. J., Bindschadler, R., Csatho, B., Farrell, S. L., Fricker, H. A., et al. (2010). The ICESat-2 laser altimetry mission. *Proceedings of the IEEE*, *98*(5), 735–751. https://doi.org/10.1109/jproc.2009.2034765

Ackley, S. (1979). Mass-balance aspects of Weddell Sea pack ice. *Journal of Glaciology*, *24*(90), 391–405. https://doi.org/10.1017/s0022143000014878

Andreas, E. L., Lange, M. A., Ackley, S. F., & Wadhams, P. (1993). Roughness of Weddell Sea ice and estimates of the air-ice drag coefficient. *Journal of Geophysical Research*, *98*(C7), 12439–12452. https://doi.org/10.1029/93jc00654

Cafarella, S. M., Scharien, R., Geldsetzer, T., Howell, S., Haas, C., Segal, R., & Nasonova, S. (2019). Estimation of level and deformed first-year sea ice surface roughness in the Canadian Arctic Archipelago from C- and L-band synthetic aperture radar. *Canadian Journal of Remote Sensing*, *45*(3–4), 457–475. https://doi.org/10.1080/07038992.2019.1647102

Carsey, F. D. (1992). *Microwave remote sensing of sea ice*. American Geophysical Union.

Cohen, A. C., & Norgaard, N. J. (1977). Progressively censored sampling in the three-parameter gamma distribution. *Technometrics*, *19*(3), 333–340. https://doi.org/10.1080/00401706.1977.10489556

Dammann, D. O., Eicken, H., Mahoney, A. R., Saiet, E., Meyer, F. J., John, C., et al. (2017). Traversing sea ice—Linking surface roughness and ice trafficability through SAR polarimetry and interferometry. *IEEE Journal of Selected Topics in Applied Earth Observations and Remote Sensing*, *11*(2), 416–433. https://doi.org/10.1109/JSTARS.2017.2764961

De Veaux, R. D., Gordon, A. L., Comiso, J. C., & Bacherer, N. E. (1993). Modeling of topographic effects on Antarctic sea ice using multivariate adaptive regression splines. *Journal of Geophysical Research*, *98*(C11), 20307–20319. https://doi.org/10.1029/93jc01503

Dierking, W. (1995). Laser profiling of the ice surface topography during the Winter Weddell Gyre Study 1992. *Journal of Geophysical Research*, *100*(C3), 4807–4820. https://doi.org/10.1029/94jc01938

Dierking, W., Carlstrom, A., & Ulander, L. M. (1997). The effect of inhomogeneous roughness on radar backscattering from slightly deformed sea ice. *IEEE Transactions on Geoscience and Remote Sensing*, *35*(1), 147–159. https://doi.org/10.1109/36.551943

Dierking, W., Lang, O., & Busche, T. (2017). Sea ice local surface topography from single-pass satellite InSAR measurements: A feasibility study. *The Cryosphere*, *11*(4), 1967–1985. https://doi.org/10.5194/tc-11-1967-2017

DLR. (2022). German Aerospace Center: Earth Observation on the Web (EOWEB) [Computer software manual]. DLR. Retrieved from https://eoweb.dlr.de

Dominguez, R. (2010). updated 2018. IceBridge DMS L1B geolocated and orthorectified images, version 1 [Computer software manual]. NSIDC. https://doi.org/10.5067/OZ6VNOPMPRJ0

Dotson, R., & Arvesen, J. (2012). updated 2014. IceBridge DMS L3 photogrammetric DEM, version 1 [Computer software manual]. NSIDC. https://doi.org/10.5067/39YO5T544XCC

Duque, S., Balss, U., Rossi, C., Fritz, T., & Balzer, W. (2012). *TanDEM-X payload ground segment, CoSSC generation and interferometric considerations*. German Aerospace Center.

Eineder, M., Fritz, T., Mittermayer, J., Roth, A., Boerner, E., & Breit, H. (2008). *TerraSAR-X ground segment, basic product specification document (Tech. Rep.)*. Cluster Applied Remote Sensing (CAF).

Farrell, S. L., Markus, T., Kwok, R., & Connor, L. (2011). Laser altimetry sampling strategies over sea ice. *Annals of Glaciology*, *52*(57), 69–76. https://doi.org/10.3189/172756411795931660

Fors, A. S., Brekke, C., Gerland, S., Doulgeris, A. P., & Beckers, J. F. (2015). Late summer Arctic sea ice surface roughness signatures in C-band SAR data. *IEEE Journal of Selected Topics in Applied Earth Observations and Remote Sensing*, *9*(3), 1199–1215. https://doi.org/10.1109/JSTARS.2015.2504384

GEBCO Compilation Group. (2020). GEBCO 2020 grid. [Computer software manual]. GEBCO. Retrieved from https://download.gebco.net/. https://doi.org/10.5285/a29c5465-b138-234d-e053-6c86abc040b9

Geiger, C. A., & Drinkwater, M. R. (2005). Coincident buoy- and SAR-derived surface fluxes in the western Weddell Sea during Ice Station Weddell 1992. *Journal of Geophysical Research*, *110*(C4). https://doi.org/10.1029/2003jc002112

Gloersen, P. (1992). *Arctic and Antarctic sea ice, 1978–1987: Satellite passive-microwave observations and analysis (No. 511). Scientific and Technical Information Program*. National Aeronautics and Space Administration.

Gow, A. J., Ackley, S. F., Buck, K., & Golden, K. M. (1987). *Physical and structural characteristics of Weddell Sea pack ice*. U.S. Army Cold Regions Research and Engineering Laboratory.

Granberg, H. B., & Leppäranta, M. (1999). Observations of sea ice ridging in the Weddell Sea. *Journal of Geophysical Research*, *104*(C11), 25735–25745. https://doi.org/10.1029/1999jc900160

Guest, P. S., & Davidson, K. L. (1991). The aerodynamic roughness of different types of sea ice. *Journal of Geophysical Research*, *96*(C3), 4709–4721. https://doi.org/10.1029/90jc02261

Haas, C., Liu, Q., & Martin, T. (1999). Retrieval of Antarctic sea-ice pressure ridge frequencies from ERS SAR imagery by means of in situ laser profiling and usage of a neural network. *International Journal of Remote Sensing*, *20*(15–16), 3111–3123. https://doi.org/10.1080/014311699211642

Harcourt, R., Hindell, M. A., Mcmahon, C. R., Goetz, K. T., Charrassin, J.-B., Heerah, K., et al. (2021). Regional variation in winter foraging strategies by Weddell seals in Eastern Antarctica and the Ross Sea. *Frontiers in Marine Science*, *8*, 1262. https://doi.org/10.3389/fmars.2021.720335

Hibler III, W., & Ackley, S. F. (1975). A sea ice terrain model and its application to surface vehicle trafficability. *Journal of Terramechanics*, *12*(3–4), 171–190. https://doi.org/10.1016/0022-4898(75)90028-2

Huang, L., & Hajnsek, I. (2021). Polarimetric behavior for the derivation of sea ice topographic height from TanDEM-X interferometric SAR data. *IEEE Journal of Selected Topics in Applied Earth Observations and Remote Sensing*, *14*, 1095–1110. https://doi.org/10.1109/jstars.2020.3036395

Hutchings, J., Heil, P., Steer, A., & Hibler, W., III. (2012). Subsynoptic scale spatial variability of sea ice deformation in the western Weddell Sea during early summer. *Journal of Geophysical Research*, *117*(C1). https://doi.org/10.1029/2011jc006961

IICWG. (2021). International Ice Charting Working Group (IICWG) overview [Computer software manual]. IICWG. Retrieved from https://nsidc.org/noaa/iicwg

Kræmer, T., Johnsen, H., & Brekke, C. (2015). Emulating Sentinel-1 Doppler radial ice drift measurements using Envisat ASAR data. *IEEE Transactions on Geoscience and Remote Sensing*, *53*(12), 6407–6418. https://doi.org/10.1109/TGRS.2015.2439044

Krieger, G., Moreira, A., Fiedler, H., Hajnsek, I., Werner, M., Younis, M., & Zink, M. (2007). TanDEM-X: A satellite formation for high-resolution SAR interferometry. *IEEE Transactions on Geoscience and Remote Sensing*, *45*(11), 3317–3341. https://doi.org/10.1109/tgrs.2007.900693

Kurtz, N. T., & Markus, T. (2012). Satellite observations of Antarctic sea ice thickness and volume. *Journal of Geophysical Research*, *117*(C8). https://doi.org/10.1029/2012jc008141

Lee, J.-S., & Pottier, E. (2009). *Polarimetric radar imaging: From basics to applications*. CRC Press.

Li, W., Cardellach, E., Fabra, F., Rius, A., Ribó, S., & Martín-Neira, M. (2017). First spaceborne phase altimetry over sea ice using TechDemoSat-1 GNSS-R signals. *Geophysical Research Letters*, *44*(16), 8369–8376. https://doi.org/10.1002/2017gl074513

Mack, S., Padman, L., & Klinck, J. (2013). Extracting tidal variability of sea ice concentration from AMSR-E passive microwave single-swath data: A case study of the Ross Sea. *Geophysical Research Letters*, *40*(3), 547–552. https://doi.org/10.1002/grl.50128

Markus, T., Massom, R., Worby, A., Lytle, V., Kurtz, N., & Maksym, T. (2011). Freeboard, snow depth and sea-ice roughness in East Antarctica from in situ and multiple satellite data. *Annals of Glaciology*, *52*(57), 242–248. https://doi.org/10.3189/172756411795931570

Massom, R. A., & Stammerjohn, S. E. (2010). Antarctic sea ice change and variability—Physical and ecological implications. *Polar Science*, *4*(2), 149–186. https://doi.org/10.1016/j.polar.2010.05.001

Millan, R., St-Laurent, P., Rignot, E., Morlighem, M., Mouginot, J., & Scheuchl, B. (2020). Constraining an ocean model under Getz Ice Shelf, Antarctica, using a gravity-derived bathymetry. *Geophysical Research Letters*, *47*(13), e2019GL086522. https://doi.org/10.1029/2019gl086522

NASA Worldview Snapshots. (2000). Terra, MODIS, corrected reflectance, true color — Aqua, MODIS, corrected reflectance, true color [Computer software manual]. NASA Worldview Snapshots. Retrieved from https://wvs.earthdata.nasa.gov

Nghiem, S. V., Borgeaud, M., Kong, J., & Shin, R. (1990). Polarimetric remote sensing of geophysical media with layer random medium model. *Progress in Electromagnetics Research*, *3*, 1–73. https://doi.org/10.2528/pier90030500

Nghiem, S. V., Busche, T., Kraus, T., Bachmann, M., Kurtz, N., Sonntag, J., et al. (2018). Remote sensing of Antarctic sea ice with coordinated aircraft and satellite data acquisitions. In *IGARSS 2018, IEEE international geoscience and remote sensing symposium* (pp. 8531–8534). https://doi.org/10.1109/igarss.2018.8518550

Nghiem, S. V., Hall, D., Rigor, I., Li, P., & Neumann, G. (2014). Effects of Mackenzie river discharge and bathymetry on sea ice in the Beaufort sea. *Geophysical Research Letters*, *41*(3), 873–879. https://doi.org/10.1002/2013gl058956

Nghiem, S. V., Huang, L., & Hajnsek, I. (2022). Theory of radar polarimetric interferometry and its application to the retrieval of sea ice elevation in the Western Weddell Sea, Antarctic. *Earth and Space Science*, *9*(5), e2021EA002191. https://doi.org/10.1029/2021ea002191

Nghiem, S. V., Kwok, R., Yueh, S., & Drinkwater, M. (1995a). Polarimetric signatures of sea ice: 1. Theoretical model. *Journal of Geophysical Research*, *100*(C7), 13665–13679. https://doi.org/10.1029/95jc00937

Nghiem, S. V., Kwok, R., Yueh, S., & Drinkwater, M. (1995b). Polarimetric signatures of sea ice: 2. Experimental observations. *Journal of Geophysical Research*, *100*(C7), 13681–13698. https://doi.org/10.1029/95jc00938

Nghiem, S. V., Rigor, I., Clemente-Colón, P., Neumann, G., & Li, P. (2016). Geophysical constraints on the Antarctic sea ice cover. *Remote Sensing of Environment*, *181*, 281–292. https://doi.org/10.1016/j.rse.2016.04.005

Nghiem, S. V., Yueh, S., Kwok, R., & Nguyen, D. (1993). Polarimetric remote sensing of geophysical medium structures. *Radio Science*, *28*(06), 1111–1130. https://doi.org/10.1029/93rs01376

NSIDC. (2022). National Snow and Ice Data Center: Distributed Active Archive Center (DAAC) IceBridge Data, NSIDC [data set] [Computer software manual]. NSIDC. Retrieved from https://nsidc.org/data/icebridge

Peterson, I., Prinsenberg, S., & Holladay, J. (2008). Observations of sea ice thickness, surface roughness and ice motion in Amundsen Gulf. *Journal of Geophysical Research*, *113*(C6). https://doi.org/10.1029/2007jc004456

Schutz, B. E., Zwally, H. J., Shuman, C. A., Hancock, D., & Di Marzio, J. P. (2005). Overview of the ICESat mission. *Geophysical Research Letters*, *32*(21). https://doi.org/10.1029/2005gl024009

Smith, W. H., & Sandwell, D. T. (2004). Conventional bathymetry, bathymetry from space, and geodetic altimetry. *Oceanography*, *17*(1), 8–23. https://doi.org/10.5670/oceanog.2004.63

Walsh, J. E. (2009). A comparison of Arctic and Antarctic climate change, present and future. *Antarctic Science*, *21*(3), 179–188. https://doi.org/10.1017/s0954102009001874

Weeks, W. F., & Ackley, S. F. (1982). *The growth, structure, and properties of sea ice (Tech. Rep.)*. Cold Regions Research and Engineering Lab.

10.1029/2022EA002472

Weeks, W. F., & Ackley, S. F. (1986). The growth, structure, and properties of sea ice. In *The geophysics of sea ice* (pp. 9–164). Springer. https://doi.org/10.1007/978-1-4899-5352-0_2

Werner, C., Wegmüller, U., Strozzi, T., & Wiesmann, A. (2000). Gamma SAR and interferometric processing software. *Proceedings of the ERS-ENVISAT symposium* (Vol. 1620, p. 1620).

WMO. (2014). *World meteorological organization sea ice nomenclature*. 5th session of JCOMM Expert Team on Sea Ice. No. 256.

Yan, Q., & Huang, W. (2019). Sea ice remote sensing using GNSS-R: A review. *Remote Sensing*, *11*(21), 2565. https://doi.org/10.3390/rs11212565

Yitayew, T. G., Dierking, W., Divine, D. V., Eltoft, T., Ferro-Famil, L., Rösel, A., & Negrel, J. (2018). Validation of sea-ice topographic heights derived from TanDEM-X interferometric SAR data with results from laser profiler and photogrammetry. *IEEE Transactions on Geoscience and Remote Sensing*, *56*(11), 6504–6520. https://doi.org/10.1109/tgrs.2018.2839590